# Melting processes, cooling rates, and tectonic settings of the Neo-Tethyan mantle: the in-situ mineral chemical record

Kai Yang, Jingen G Dai, Jie Shen, Baptiste Debret

▶ **To cite this version:**

Kai Yang, Jingen G Dai, Jie Shen, Baptiste Debret. Melting processes, cooling rates, and tectonic settings of the Neo-Tethyan mantle: the in-situ mineral chemical record. Chemical Geology, 2024, 643, pp.121834. 10.1016/j.chemgeo.2023.121834 . hal-04304221

**HAL Id: hal-04304221**
**https://hal.science/hal-04304221**

Submitted on 24 Nov 2023

**HAL** is a multi-disciplinary open access archive for the deposit and dissemination of scientific research documents, whether they are published or not. The documents may come from teaching and research institutions in France or abroad, or from public or private research centers.

L'archive ouverte pluridisciplinaire **HAL**, est destinée au dépôt et à la diffusion de documents scientifiques de niveau recherche, publiés ou non, émanant des établissements d'enseignement et de recherche français ou étrangers, des laboratoires publics ou privés.

Journal Pre-proof

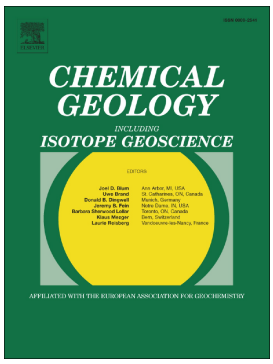


# Melting processes, cooling rates, and tectonic settings of the Neo-Tethyan mantle: The in-situ mineral chemical record

Kai Yang, Jingen Dai, Jie Shen, Baptiste Debret

PII: S0009-2541(23)00535-1

DOI: https://doi.org/10.1016/j.chemgeo.2023.121834

Reference: CHEMGE 121834

To appear in: *Chemical Geology*

Received date: 18 July 2023

Revised date: 7 November 2023

Accepted date: 15 November 2023

Please cite this article as: K. Yang, J. Dai, J. Shen, et al., Melting processes, cooling rates, and tectonic settings of the Neo-Tethyan mantle: The in-situ mineral chemical record, *Chemical Geology* (2023), https://doi.org/10.1016/j.chemgeo.2023.121834

This is a PDF file of an article that has undergone enhancements after acceptance, such as the addition of a cover page and metadata, and formatting for readability, but it is not yet the definitive version of record. This version will undergo additional copyediting, typesetting and review before it is published in its final form, but we are providing this version to give early visibility of the article. Please note that, during the production process, errors may be discovered which could affect the content, and all legal disclaimers that apply to the journal pertain.

© 2023 Published by Elsevier B.V.

Journal Pre-proof

# Melting processes, cooling rates, and tectonic settings of the Neo-Tethyan mantle: the *in-situ* mineral chemical record

Kai Yang[1, 2], Jingen Dai[1†], Jie Shen[1], Baptiste Debret[2]

[1]School of Earth Science and Resources, State Key Laboratory of Geological Processes and Mineral Resources, Research Center for Tibetan Plateau Geology, China University of Geosciences, Beijing, China

[2]Université Paris Cité, Institut de physique du globe de Paris, CNRS, Paris, France

†Corresponding author: J.G. Dai (djgtibet@163.com)

Journal Pre-proof

Journal Pre-proof


## Abstract

Peridotites in the Yarlung Zangbo ophiolite (YZO) have the potential to elaborate the mantle dynamics that operated below the Neo-Tethyan oceanic crust. Here, we measured major and trace element concentrations of minerals (e.g., clinopyroxene, orthopyroxene, olivine, and spinel) in YZO harzburgites and lherzolites to trace the origin and evolution of the YZO. The rare earth element (REE) patterns of clinopyroxenes in lherzolites and harzburgites plot within the field of abyssal and forearc peridotites, respectively, indicating that the latter experienced a higher degree of partial melting. Based on the relative extents of light (LREE) and heavy (HREE) REE depletions in clinopyroxene, we classified the lherzolites into two groups (I and II). The group I clinopyroxenes are depleted in HREEs and enriched in LREEs and MREEs compared to those of group II. Meanwhile, the REE patterns of harzburgite clinopyroxenes are identical to that of group II, although they display lower REE concentrations. Models based on REE abundances in clinopyroxene suggest that group I lherzolites experienced ~8–11% partial melting in the spinel domain, whereas group II lherzolites formed after 5% melting in the garnet domain followed by 6–9% and 9-16% partial melting in the spinel domain, respectively. These high degrees of melting may suggest that the harzburgites formed in a supra-subduction zone (SSZ) setting. Surprisingly, the REE-in-two-pyroxenes thermometer ($T_{REE}$) shows that the YZO peridotites record high-temperature cooling at 991–1218 °C which is lower than the conditions below mid-oceanic ridges (MORs), but compatible with recent reports of high closure temperatures in forearc environments. Furthermore, our $T_{REE}$ results constrain the cooling rate of the YZO peridotites to ~0.01–0.5 °C/yr, overlapping with rates reported for SSZ, MOR, and abyssal peridotites. By integrating the petrological, geochemical, and thermal features, we tentatively interpret the group I lherzolites accreted in an Early Cretaceous forearc during subduction initiation, whereas the group II lherzolites and the harzburgites formed by further melting of the earlier lherzolites in a SSZ setting.


**Key words**: Yarlung Zangbo suture zone; Ophiolite; Peridotite; Melting process; Cooling rates

Journal Pre-proof

Journal Pre-proof

# 1. Introduction

Ophiolites are remnants of the oceanic lithosphere (Dewey and Bird, 1971; Coleman, 1977; Nicolas, 1989; Dilek and Furnes, 2011), which is generated either at mid-ocean ridges (MORs) or in supra-subduction zones (SSZs). Consequently, investigations of ophiolites worldwide often demonstrate a combination of MOR and SSZ features in either an extensional or compressional setting; this phenomenon is termed the "ophiolite conundrum" (Moores et al., 2000; Metcalf et al., 2008). One possible explanation lies in the diverse interpretations of the geochemical compositions of ophiolite crustal rocks. However, because ophiolites typically comprise both mantle and crustal rocks, peridotites in the mantle sections offer valuable insights into the chemical and physical processes influencing the upper mantle under various tectonic conditions (Hanghøj et al., 2010; Dilek and Furnes, 2011).

Tethyan ophiolites have been critical in shaping our understanding of ophiolite evolution over the past centuries, offering numerous compelling instances of the ophiolite conundrum (Moores et al., 2000; Dilek and Furnes, 2019). These examples show a remarkable diversity of crustal-mantle structures and compositions, and extend from the western Mediterranean to the Tibetan Himalayas (Lagabrielle and Cannat, 1990; Smith, 1993; Dilek and Moores, 1990, 2019; Moores et al., 2000). The Yarlung Zangbo ophiolite (YZO) is the youngest Tethyan ophiolite on the Tibetan Plateau, capturing a continuous record from the opening of the Neo-Tethys to its subduction and the subsequent collision of India and Eurasia. The YZO thus contains well-preserved Neo-Tethyan oceanic mantle and crustal rocks. The mantle peridotite is dominated by variably serpentinized harzburgite with minor dunite and lherzolite (Girardeau et al., 1985; Hébert et al., 2003; Nicolas et al., 1981) that can provide crucial insights into the evolutionary history of melts, including melting and melt extraction processes and melt-rock interactions (Prinzhofer and Allègre, 1985; Kelemen et al., 1992; Zhou et al., 2005; Arai et al., 2007; Dilek et al., 2007; Ishikawa et al., 2007; Eyuboglu et al., 2010; Dai et al., 2011; Xiong et al., 2017).

Similar to other ophiolites globally, the tectonic setting of the YZO remains debated. On one hand, based on structural similarities to the ultraslow Southwest Indian Ridge and the Ligurian ophiolite, the YZO may have originated in a slowly or ultraslowly spreading MOR (Nicolas et al., 1981; Girardeau and Mercier, 1988; Pearce et al., 1988; Wu et al., 2014; C.Z. Liu et al., 2014; T.

Liu et al., 2016; Zhang et al., 2016). On the other hand, the YZO may have been generated in a SSZ setting, a scenario for which three models have been proposed: (1) the YZO formed along a forearc that was spreading *via* rapid accretion associated with subduction initiation from ~130 Ma to 120 Ma (Malpas et al., 2003; Dai et al., 2013; An et al., 2014; Huang et al., 2015; Maffione et al., 2015); (2) it was initially generated in a MOR setting and subsequently modified in a SSZ through subduction initiation (Zhou et al., 1996, 2005; Aitchison et al., 2000; Malpas et al., 2003; Dubois-Côté et al., 2005; Liu et al., 2010; Xu et al., 2011; Hébert et al., 2012; Su et al., 2015); and (3) it experienced a two-stage forearc accretion in which asthenospheric lherzolites were accreted onto a depleted harzburgite forearc during subduction initiation (Xiong et al., 2016, 2017). Therefore, further evidence is needed to better constrain the origin and evolution of the YZO. In particular, the degree of partial melting and the cooling rate of peridotites differ between MOR and SSZ mantle domains, and thus may be useful in unraveling the ophiolite conundrum in the case of the YZO. However, this requires a systematic framework of partial melting and cooling rates along the Yarlung Zangbo Suture Zone (YZSZ, Fig. 1), which has yet to be established.

In this study, we report comprehensive petrographic observations and chemical compositions of clinopyroxene, orthopyroxene, olivine, and spinel from Zedang, Xigaze, and Zhongba ophiolitic peridotites in the eastern, central, and western regions of the YZSZ, respectively. From these, we determined degrees of depletion, closure temperatures, and cooling rates for mantle peridotites in the YZO. These results provide a new perspective to the ophiolite conundrum and should prove useful in determining the thermal and dynamic processes that took place within the Neo-Tethyan oceanic mantle.

## 2. Geological setting and sample descriptions

The Tibetan Plateau is composed of four major terranes: the Himalaya, Lhasa, Qiangtang, and Songpan-Ganzi from south to north. These terranes are separated by four major suture zones: the YZSZ, Bangong-Nujiang Suture Zone (BNSZ), Jinshajiang Suture Zone (JSSZ), and A'nemaqin-Kunlun Suture Zone (AKSZ) from south to north (Fig. 1; Yin and Harrison, 2000). The YZSZ, the youngest suture of the Tibetan Plateau, is an east–west trending belt >2,000 kilometers long between the Indian and Lhasa terranes (Fig. 1; Yin and Harrison, 2000). The Gangdese arc to the north of the YZSZ records four main magmatic episodes during 205–152 Ma, 109–80 Ma, 65–41Ma, and 33–13 Ma (Ji et al., 2009; Zhu et al., 2011, 2013), caused by the

Journal Pre-proof

subduction of the Neo-Tethys beneath the Lhasa terrane (Ji et al., 2009; Zhu et al., 2011, 2013; Xiong et al., 2016). To the south of the YZSZ, the Tethyan Himalayan sequence represents the northernmost part of the Indian continental margin; it comprises extensive magmatic rocks that originated from the Kerguelen plume beneath eastern Gondwana and were emplaced during the Early Cretaceous (Zhu et al., 2009; Wang et al., 2018; Yang et al., 2022).

The YZO represents remnants of the Neo-Tethyan oceanic lithosphere emplaced within the YZSZ (Fig. 1). Previous studies demonstrated that the YZO was accreted along the Gangdese arc from the Late Jurassic to Early Cretaceous (Allégre et al., 1984; Aitchison et al., 2000; Hébert et al., 2012; Dai et al., 2013, 2021; Wu et al., 2014; Liu et al., 2016; Zhang et al., 2016). The YZO is divided into three segments from east to west (Hébert et al., 2012). The eastern segment contains the ophiolitic massifs of Nang, Luobusha, and Zedang, which are characterized by large mantle sequences, including harzburgite and dunite. The andesite, gabbro, and diabase from Luobusha-Zedang have marked large-ion lithophile element (LILE) compositional anomalies relative to the other segments of the YZO, suggesting a continental component (subducted sediments) in the source of this ophiolite segment (Hébert et al., 2012). In its central segment, the YZO is also called the Xigaze ophiolite, which includes ophiolitic complexes in Renbu, Dazhuqu, Luqu, Jiding, Ngamring, and Sangsang. These are characterized by large mantle units comprising harzburgite and lherzolites, and are associated with minor gabbros and volcanic and/or sedimentary units of variable thickness. The western segment of the YZO comprises Saga, Zhongba, Dangqiong, Xiugugabu, Purang, and Dongpo. These ophiolite sequences mainly consist of mantle peridotites within mélange zones. Overall, the YZO is characterized by thin crustal sections (Shi et al., 2007, 2012; Gong et al., 2016) containing sporadic mafic dikes and volcanic rocks with MORB affinities.

The above characteristics have led several studies to propose that the YZO was in a slow- to ultraslow-spreading setting before being accreted onto the continent (Girardeau and Mercier, 1988; Wu et al., 2014; C.Z. Liu et al., 2014; Zhang et al., 2016; T. Liu et al., 2021). Recently, however, abundant geochemical data suggest that the ophiolite was generated in a SSZ setting based on three lines of evidence. (1) YZO peridotites have refractory compositional features including U-shaped whole-rock REE patterns and high spinel Cr# values (Hébert et al., 2003; Dai et al., 2013; Xiong et al., 2017), suggesting that they underwent hydrous melting before their

exposure. In addition, Xiong et al, (2016) identified that YZO lherzolites have higher equilibration temperatures than YZO harzburgites, which they attributed to the two-stage subduction-related accretion of the Zedang lherzolite and harzburgite during 200–130 Ma and 130–120 Ma, respectively. (2) Mafic and felsic rocks of the YZO have wide ranges of incompatible element concentrations that are similar to those of SSZ-related volcanics (Zhou et al., 2005; Hébert et al., 2012; Dai et al., 2011, 2013, 2021; Huang et al., 2015; Su et al., 2015). (3) Field observations reveal that the sediments of the Xigaze fore-arc basin were directly overlain by the YZO immediately after extension ceased (An et al., 2014; Dai et al., 2015, 2021; Wang et al., 2012), that the YZO formed near the Asian continental margin (Huang et al., 2015), and that the associated magmatic arc, the Cretaceous Gangdese batholith, lies well to the north of the YZO (Dai et al., 2021). Otherwise, ultrahigh pressure minerals (including diamond, moissanite, wüstite, Fe-silicides, and Fe-Ni-Cr-PGE alloys requiring minimum pressures of ~2.8–4 GPa) in the spinel phase of the YZO (Robinson et al., 2004; Yang et al., 2007, 2014) have been interpreted as older material (~230 Ma) incorporated during seafloor spreading (Ruskov et al., 2010).

The samples studied herein encompass the western (Zhongba), middle (Xigaze), and eastern (Zedang) sections of the YZO. Those from Zhongba and Xigaze predominantly consist of harzburgite, whereas the Zedang samples are mainly lherzolite (Fig. 1). The Zhongba ophiolitic harzburgites are thrust over diabase dikes and pillow basalts that are surrounded by a mélange zone comprising limestone, chert, and massive basalt. The Xigaze peridotite is well preserved and has not been subjected to significant dismembering during emplacement. It comprises chromite-bearing harzburgite, serpentinite, and minor dunite, and has been intruded by numerous mafic dikes. The Zedang peridotite massif consists of lherzolite and harzburgite from west to east and adjacent to crustal mélanges (Fig. 1b).

The YZO harzburgites display a weak foliation underlined by oriented orthopyroxene porphyroclasts (Fig. 2a; Pirard et al., 2013) and porphyroclastic microstructures (Fig. 3a, c). Compared to the lherzolites, they have higher modal olivine (~65–80 vol.%) and orthopyroxene contents (~18–35 vol.%), lower modal clinopyroxene contents (~0.5–3.5 vol.%), and similar model spinel contents (~2–3 vol.%). Thin sections show that these rocks are relatively fresh, with <5% serpentinization (Fig. 3a–c). They show millimeter-sized porphyroclasts of orthopyroxene (Opx1), olivine (Ol1), and clinopyroxene (Opx1) that are surrounded by fine-grained matrix

assemblages (e.g., Opx2, Ol2, Cpx2, Spl, magnetite, serpentine, sulfide; Fig. 3b, d). Olvine porphyroclasts (Ol1) are weakly deformed, showing undulatory extinction, and are fragmented (Fig. 3a). Orthopyroxene porphyroclasts (Opx1) display undulatory extinction, curved cleavages, have Cpx exsolution lamellae, and occur in close spatial association with spinel (Fig. 3a, b, l). Clinopyroxene porphyroclasts (Cpx1) exhibit curvilinear margins and lack plastic deformation features (Fig. 3c). Spinel grains are brown and usually display holly-leaf-shaped and vermicular textures (Fig. 3c).

The lherzolites display porphyroclastic textures (Fig. 3d, e). comprise olivine (~58–67 vol.%), orthopyroxene (~20–30 vol.%), clinopyroxene (~5–8 vol.%), and minor spinel (~2–4 vol.%), and are remarkably fresh with <1% serpentinization (Fig. 3d–f). Olivine porphyroclasts can reach ~8 mm in diameter and exhibit undulatory extinction with irregular margins (Fig. 3f). Olivine granoblasts are 20–300 μm wide in interstitial spaces. Orthopyroxene porphyroclasts locally reach ~12 mm in diameter and have embayed margins compatible with features resulting from partial melting. Finer minerals (Ol2, Opx2) surrounding the porphyroclasts (Ol, Opx, and Cpx) were subjected to intensive melt/rock reactions, as shown by Figure 3d. Porphyroclastic clinopyroxenes can be as large as ~7 mm in diameter, and exhibit irregular shapes with undulatory extinction (Fig. 3f). As in the harzburgites, exsolution is well developed in both Cpx1 and Opx1, but rarely observed in Cpx2 and/or Opx2 (Fig. 3e, f), indicating that the porphyroclastic pyroxenes in both the harzburgites and lherzolites are residual crystals formed by partial melting of the asthenosphere (Xiong et al., 2015).

# 3. Analytical Methods

## 3.1 *In-situ* electron microprobe analyses

Electron microprobe analyses of peridotite minerals (pyroxenes, olivine, and spinels) were performed using a JEOL JXA-8230 electron probe microanalyzer (EPMA) at the Key Laboratory of Mineralogy and Metallogeny, Guangzhou Institute of Geochemistry, Chinese Academy of Sciences and at the Sample Solution Analytical Technology Co., Ltd., Wuhan, China. Analyses were conducted at 15 kV accelerating voltage and 20–25 nA beam current with a focused beam (1 μm diameter). On-peak and background counting times were 20 s and 10 s, respectively, for Ti,

Na, Mn, K, and Cr, and 10 s and 5 s, respectively for Si, Ca, Mg, Al, Fe, P, V, and Ni. The ZAF correction method in the JEOL software was used to calibrate the peaks. Detection limits for major elements were 75–350 ppm. Analytical precision was better than 1%, 5%, and 10% when major element contents exceeded 10 wt.%, 1 wt.%, and 0.1 wt.%, respectively. Mineral major element contents are reported in Table S1.

### 3.2 *In-situ* trace element analyses by LA-ICP-MS

*In-situ* trace element analyses of olivine, orthopyroxene, and clinopyroxene were performed by laser ablation inductively coupled plasma mass spectrometry (LA-ICP-MS) at the Sample Solution Analytical Technology Co., Ltd., Wuhan, China. Minerals were ablated using a GeolasPro laser system with a wavelength of 193 nm and a maximum energy of 200 mJ. An Agilent 7700e ICP-MS was used to acquire ion signal intensities at a frequency of 5 Hz. Analytical spots were 44 μm in diameter, resulting in a laser energy density on the mineral surface of 5.5 J/cm$^2$. Acquisition times *per* spot included 20–30 s of background acquisition followed by 50 s of ablation and data acquisition. The BHVO-2G and BIR-1G glass reference materials were used as external calibration standards and sample $^{28}$Si was selected as an internal standard to calibrate mineral trace element compositions. Within errors, the calibration Si values of BHVO-2G and BIR-1G agreed with those of Liu et al. (2008), and those of our samples with the Si contents obtained by EPMA (Table S1). We used the Excel-based software ICPMSDataCal to perform off-line selection and integration of background and analyzed signals, time-drift correction, and quantitative calibration for trace element analyses (Liu et al., 2008).

Additional LA-ICP-MS analyses were performed using a NewWave 193UC excimer laser ablation system and Agilent 7900 ICP-MS at the Mineral Laser Microprobe Analysis Laboratory (Milma Lab), China University of Geosciences, Beijing, China. Detailed instrumental and analytical settings are reported in Zhang et al. (2019) and summarized here. Analyses were performed using a spot size of 75 μm, a repetition rate of 8 Hz, and ablation time of 40 s, and laser energy density on the mineral surface of 4 J/cm$^2$. Quantitative data calibration was performed using the Iolite software on Igor (Paton et al., 2011). The NIST 610 glass reference material was used as an external calibration standard and $^{28}$Si was selected as an internal standard. The Si content of NIST 610 is from Jochum et al. (2011) and sample Si contents were compared with those determined by EPMA. The USGS reference glass BCR-2G was analyzed as a secondary

standard to validate the accuracies of both laboratories' measurements. Slight deviations in elemental concentrations were observed in the 2RSD values (Relative Standard Deviation, $2\text{RSD} = \frac{2*\sqrt{\frac{\sum_{i=1}^{n}(x_i-\bar{x})^2}{n-1}}}{\bar{x}} \times 100\%$) of replicate analyses from both laboratories. Upon analysis, we observed that the 2RSD values for Li, Na, Al, K, Sc, Ti, V, Co, Rb, Sr, Y, Zr, Nb, Cs, Ba, La, Ce, Pr, Nd, Sm, Eu, Gd, Er, Hf, and Pb were nearly identical at <6%, whereas those for Ca, Cr, Ni, Dy, Ho, Tm, Yb, Lu and Ta were in the range 6–10% (Table S1). However, because the standard values obtained from both laboratories suggest were consistent with the recommended values within errors, we consider these 2RSD values to be within the acceptable margin of error (Jochum et al., 2005; Liu et al., 2008).

# 4. Results

## 4.1. Mineral major and trace element compositions

### 4.1.1. Olivine and Spinel

Olivine porphyroclasts in lherzolites have Mg# (= 100 × Mg/(Mg + $Fe_{Tot}$)) = 90.0–91.1 (mean 90.3) and contained 8.6–9.6 wt.% FeO, whereas those in harzburgites were only slightly more magnesian (Mg# = 90.4–91.5, mean 90.8) and contained only slightly less FeO (8.3–9.4 wt.%) (Table S1). Spinel grains in lherzolites contained 39.10–47.54 wt.% $Al_2O_3$ and 13.65–15.99 wt.% FeO, with Mg# = 63.79–69.61 and Cr# (= 100 × Cr/(Cr + Al)) = 20.26–32.50, whereas those in harzburgites contained less $Al_2O_3$ (32.20–40.60 wt.%), more FeO (14.71–17.01 wt.%), and were less magnesian (Mg# = 60.04–65.23) and more chromian (Cr# = 31.78–41.66) ( Table S1; Fig. 4).

Olivine Mg# and Cr# values in harzburgites and lherzolites are not distinctly different, whereas spinel Mg# and Cr# values differ between the two lithologies (see Table S1; Fig. 4a). Plotting olivine Mg# versus spinel Cr# shows that the harzburgites span the boundary between the SSZ and abyssal peridotite fields, whereas lherzolites plot exclusively within the abyssal field (Fig. 4b). Although trace element data for olivine have been reported (Aulbach et al., 2017), most of the olivine trace element concentrations obtained herein were below the detection limit in both harzburgites and lherzolites. Therefore, we do not discuss olivine REE or trace element contents in any further detail (Table S1).

Journal Pre-proof

Journal Pre-proof

#### 4.1.2. Clinopyroxene

Porphyroclastic clinopyroxenes in harzburgites contain less $TiO_2$ (0.01–0.11 wt.%) and more CaO (18.72–24.91 wt.%) than those in lherzolites (0.01–0.17 wt.% $TiO_2$ and 13.33–24.42 wt.% CaO, respectively). They also had MgO (15.68–23.35 wt.%), $Al_2O_3$ (1.94–4.48 wt.%), and FeO contents (1.82 wt.%-3.44 wt.%) similar to those in lherzolites (15.21–22.51 wt.% MgO, 1.61–4.67 wt.% $Al_2O_3$, and 1.63–4.23 wt.% FeO, respectively; Table S1). We observed a positive correlation between clinopyroxene $Cr_2O_3$ and $Al_2O_3$ contents, and a negative correlation between clinopyroxene MgO and $Al_2O_3$ content (Fig. 5a, b).

The REE and trace element distributions of clinopyroxenes in lherzolites and harzburgites are shown in Figure 6. In addition, we compiled Cpx data in YZO peridotites from previous studies and combined it with the results presented in this study to more accurately determine the conditions of partial melting (Fig. 7-9). Clinopyroxenes in lherzolites were strongly depleted in LREEs relative to HREEs (average ΣHREE/ΣLREE = 12.67; Fig. 6a). In contrast, clinopyroxenes in harzburgites were relatively enriched in LREEs and LILEs (Fig. 6c). These distinct patterns were previously reported in abyssal and forearc settings, respectively (Fig. 6a, c). In addition, clinopyroxenes in lherzolites can be divided into two groups according to their major element and REE compositions. Group I lherzolite clinopyroxenes exhibit higher $Na_2O$ contents (average 0.35 wt.%) than those of group II (average 0.09 wt.%; Fig. 5d). Additionally, group I clinopyroxenes are depleted in HREEs and enriched in LREEs and MREEs (average Yb/La, Yb/Nd, and Yb/Gd ratios of 150.9, 3.7, and 1.7, respectively) compared to those of group II (196.2, 38.9, and 2.2, respectively; Fig. 6a). These distinguishing characteristics highlight the contrasting geochemical features of group I and II clinopyroxenes.

#### 4.1.3. Orthopyroxene

Orthopyroxenes in harzburgites contained less $Al_2O_3$ (1.90–3.63 wt.%) than those in lherzolites (1.78–5.04 wt.%), but had similar concentrations of MgO (27.72–36.02 wt.%), FeO (4.62–6.88 wt.%), and CaO (0.34–3.82 wt.%) to those in lherzolites (30.90–34.29 wt.% MgO, 4.99–6.90 wt.% FeO, and 0.21–3.89 wt.% CaO, respectively). Orthopyroxene REE concentrations were below chondritic values in both lherzolites and harzburgites, defining a clear left-skewed pattern characteristic of LREE enrichment comparing harzburgites to lherzolites (Fig. 6a, c).

Journal Pre-proof

Orthopyroxenes in harzburgites were enriched in high-field-strength elements (HFSEs) and had positive U, Ta, Pb, Ti, and Li anomalies (Fig. 6c, d). Orthopyroxene LILE contents in harzburgites were similar to or higher than those in coexisting clinopyroxene (Fig. 6d; see next subsection). Orthopyroxenes in lherzolites had similar middle to heavy REE (MREE-HREE) contents as those in harzburgites, but lacked positive La and Ce anomalies and had lower HFSE contents (Fig. 6a, c).

## 4.2. Equilibration temperature and cooling rate of YZO peridotites

Various geothermometers are currently available to evaluate the thermal histories of mafic or ultramafic rocks. These geothermometers can be divided into two types according to whether they are based on mineral major element (Wells, 1977; Brey and Köhler, 1990; Witt-Eickschen and Seck, 1991; Taylor, 1998; MacGregor, 2015) or trace element concentrations (Liang et al., 2013). Accordingly, the major and trace element compositions of coexisting Cpx-Opx pairs can be used to calculate the equilibrium temperature. Broadly applied major element geothermometers calculate temperature based on the distribution of Ca (Lindsley and Andersen, 1983; Brey and Köhler, 1990; referred to as $T_{BKN}$) and Fe-Mg exchange (Wells, 1977; Putirka, 2008) between Cpx-Opx pairs. Recently, the REE-in-two-pyroxenes thermometer was developed by Liang et al. (2013), which uses parameterized lattice-strain models for REE and Y (REE+Y) partitioning between two pyroxenes and a basaltic melt to calculate temperature ($T_{REE}$). Because the equilibrium Fe-Mg diffusivities are higher than Ca, which is higher than REE between two pyroxenes (Liang et al., 2013), $T_{REE}$ may record near-peak or magmatic temperatures, whereas $T_{BKN}$ records relatively lower temperatures, i.e., during cooling (Liang et al., 2013; Dygert and Liang, 2015). By relying on the diffusivities of mineral components, these thermometers provide valuable insights into both the cooling of mantle peridotites and the mechanisms involved in their emplacement. Here, we employed the REE+Y thermometer to try to evaluate the near-peak or magmatic equilibrium temperatures of YZO peridotites. We chose equilibrated Cpx-Opx pairs that exhibited well-defined contact margins and compositional homogeneity from core to rim (Fig. 3; Liang et al., 2013; Secchiari et al., 2022). To ensure higher accuracy and reduce standard deviations, we employed a larger laser beam spot (75 μm diameter) when acquiring the trace element concentrations of these mineral pairs.

The distributions of $T_{REE}$ and $T_{BKN}$ in mantle samples from different geotectonic settings are

shown in Figure 9. The equilibration temperatures of many peridotites show an apparent difference between $T_{BKN}$ and $T_{REE}$ (Fig. 9) that can be attributed to the distinct diffusion rates of divalent (e.g., $Mg^{2+}$, $Ca^{2+}$, and $Fe^{2+}$) and trivalent cations (e.g., $Al^{3+}$, $Cr^{3+}$, and $REE^{3+}$) during sub-solidus cooling (Liang et al., 2013). Here, we used $T_{BKN}$ and $T_{REE}$ to better evaluate the thermal histories of peridotites in the YZO. Temperature estimates are reported in Table S2.

$T_{BKN}$ is broadly lower than $T_{REE}$ in YZO peridotites. Group I lherzolites yielded a tighter range of $T_{BKN}$ (884–977 °C) than group II lherzolites and harzburgites (836–977 °C). In contrast, $T_{REE}$ ranges for group I lherzolites and group II and harzburgites were relatively similar, at 994–1162 °C, 991-1103 °C and 991–1218 °C, respectively. On median, the YZO group II lherzolites and harzburgites display similar $T_{BKN}$ (917 ± 40 °C, 1 sd) and $T_{REE}$ (1137 ± 61 °C, 1 sd) to the group II lherzolites ($T_{BKN}$ = 935 ± 30 °C and $T_{REE}$ = 1110 ± 58 °C, respectively; Fig. 9g, h). Group I lherzolites have slightly higher $T_{BKN}$ (935 ± 30 °C, 1sd) and $T_{REE}$ (1110 ± 58 °C, 1sd) than group II lherzolites (903 ± 28 °C and 1077 ± 47 °C 1sd, respectively; Table S2). These $T_{REE}$ values are negatively correlated with clinopyroxene $TiO_2$ contents (Fig. 10b) but positively correlated with CaO (Fig. 10c).

# 5. Discussion

## 5.1 Melting process of the YZO peridotites

Ophiolitic peridotites preserve a record of melt extraction and melt-rock interaction processes affecting the upper mantle prior to their exhumation. Therefore, the YZO has the potential to provide new insights into the evolution of the Neo-Tethys Ocean. Peridotite bulk rock data are often affected by late processes such as retrograde metamorphism, serpentinization, and/or alteration, complicating the interpretation of REE and trace element patterns. In contrast, *in-situ* analyses of unaltered minerals can help constrain mantle processes affecting peridotites prior to their alteration near the surface (Johnson et al., 1990). The degree of peridotite partial melting can be traced using the relative abundances of incompatible elements (Zr, Ti, Nd, and REEs) in silicate minerals. In particular, compared to olivine, pyroxenes are quite resistant to serpentinization (Martin and Fyfe, 1979) and their incompatible element concentrations are often used to decipher melt/rock interaction processes affecting peridotites at high temperatures (Aldanmaz et al., 2009; Birner et al., 2017; Bizimis et al., 2000; Johnson et al., 1990). In the YZO peridotites, two

generations of pyroxenes are distinguished petrographically: porphyroclastic and finer pyroxenes. Of those, the porphyroclasts (Cpx1 and Opx1) display large grains, weak deformation, irregular margins, and exsolution lamellae, indicating them to be residual pyroxenes formed by partial melting.

Clinopyroxenes and orthopyroxenes in YZO harzburgites show lower $Al_2O_3$, CaO, $TiO_2$ concentrations and higher MgO and NiO concentrations than those in lherzolites, consistent with forearc peridotites worldwide. In comparison, the compositions of the group I and group II lherzolites are consistent with those of abyssal peridotites formed by anhydrous melting, as evidenced by their similar spinel Cr# and Mg# values (Fig. 4a), olivine Mg# values (Fig. 4b), and clinopyroxene Ti contents (Fig. 5c). Spinel Cr# values are generally used to evaluate the extent of partial melting of mantle peridotites as $F = 10 \times (\ln \text{Cr\#}) + 24$, where $F$ is the degree of fractional melting; note that this formula only applies for Cr# values between 0.1 and 0.6 (Hellebrand et al., 2001). Accordingly, the extents of partial melting of the studied harzburgites and lherzolites are 14–22% and 12–16%, respectively (Fig. 4c). However, because spinel compositions are susceptible to refertilization during subsequent melting events, these degrees of melting may be underestimates (Secchiari et al., 2016, 2020). The degree of mantle peridotite depletion can also be traced *via* clinopyroxene REE concentrations (Johnson et al., 1990). In contrast to LREE and MREEs, HREEs in clinopyroxenes are not affected by alteration and serpentinization (Vernières et al., 1997; Niu, 2004). Therefore, clinopyroxene HREE concentrations can be used to further constrain the degree of partial melting.

Several studies have already used clinopyroxene REE concentrations to constrain the extent of partial melting of the YZO peridotite (Xiong et al., 2017; Zhang et al., 2017, 2020; Liu et al., 2019). Their evaluation focused on the peridotites located to the east of Xigaze, revealing variable partial melting extents in peridotites ranging from 7 to 20%. In detail, clinopyroxenes in the Luqu harzburgite display relatively flat HREE distributions that Zhang et al. (2017) attributed to 15–20% fractional melting of a depleted MORB mantle (DMM) in the spinel stability field. Clinopyroxenes in the Dazhuqu lherzolite and harzburgite have similar MREE and HREE patterns relative to that described in Liu et al. (2019). Clinopyroxenes in the Zedang lherzolite and harzburgite show different REE patterns, with lherzolitic clinopyroxenes exhibiting higher MREE and HREE concentrations and lower LREE concentrations than harzburgitic clinopyroxenes. Xiong et al. (2017) proposed that the Zedang lherzolites experienced 7–12% fractional melting

Journal Pre-proof

whereas the harzburgites were formed through 13–19% fractional melting of a DMM source within the spinel stability field. Zhang et al. (2020) reported similar REE patterns in Luobusha and modelled a degree of partial melting under spinel facies conditions to be <15%. Indeed, although their studies greatly contributed to our comprehension of the degree of partial melting of the YZO peridotites, those calculations were based solely on REE contents and were conducted solely for the spinel field, and did not match well with sample observations. Therefore, a more accurate constraint on the degree of partial melting of the mantle peridotite is essential. Here, we integrated previously reported data with our new samples from the western, central, and eastern parts of the YZO. We employed a variety of methods to estimate the extent of partial melting, thereby providing a more comprehensive and systematic understanding of the depletion of the YZO peridotites. We compared results from two non-modal fractional melting models, namely single-stage anhydrous melting, and two-stage anhydrous melting. We used clinopyroxene REE concentrations to evaluate the extent of partial melting. Starting compositions and melting modes are from Johnson (1998), and the melting equations and mineral-melt partition coefficients are from Hellebrand et al. (2002).

We first modeled changes to clinopyroxene REE patterns during partial melting in either the spinel facies or the garnet facies (Fig. 7). In the spinel stability field, REE distributions in group I and II clinopyroxenes in lherzolites require a lower degree of fractional melting (5–15%) than clinopyroxenes in harzburgites (10–20%; Fig. 7a, b). Group I lherzolitic clinopyroxenes are well fit by 8–11% fractional melting (Figure. 7a). However, harzburgitic and group II lherzolitic clinopyroxenes do not match the REE distributions expected during melting under spinel or garnet stability (Fig. 7). This result indicates that the harzburgites and group II lherzolites of the YZO could not have formed by a single stage of fractional melting under anhydrous conditions.

Compared to clinopyroxenes in group I lherzolites, the lower HREE concentrations and flatter HREE patterns of those in group II lherzolites and harzburgites indicate that they may experience higher degrees of melting and were influenced by garnet phases (Fig. 6a, c). In addition, garnet and ultrahigh pressure minerals (e.g. diamond, moissanite, wüstite, alloys) are discovered in the peridotites of YZO, indicating these peridotites might have originated from a deep source (Robinson et al., 2004; Yang et al., 2007, 2014; Gong et al., 2020). Therefore, we used a combination of melting in the garnet stability field and additional melting under the spinel stability field to better model partial melting of the group II lherzolites and harzburgites (Fig. 8).

This two-stage model shows that the group II lherzolites and harzburgites are well fit by an initial 5% partial melting in the garnet field followed by 6–9% and 9–16% partial melting in the spinel field, respectively (Fig. 8). The group II lherzolites and harzburgites clearly experienced higher degrees of partial melting than the group I lherzolites. Both petrographic and chemical evidence indicate the YZO harzburgites to refractory lithotypes, whereas the group I and group II lherzolites are relatively fertile. There is also evidence for an increase degree of partial melting rates passing from group I lherzolites to group II lherzolites and harzburgites. These differences indicate that that each lithology formed under different temperature and pressure conditions, and potentially in different geodynamic environments.

## 5.2 The processes of LREE enrichment

The occurrence of secondary vermicular or fine-grained minerals in peridotite indicates its formation *via* melt-rock interaction (Kaczmarek and Müntener, 2008; Xiong et al., 2017), a process that can impact clinopyroxene LREE concentrations (Müntener et al., 2004; Le Roux et al., 2007; Piccardo et al., 2007). Secondary minerals (Cpx2, Opx2, Ol2) are observed in both harzburgites and lherzolites in the YZO (Fig. 3a–f), whereas Cpx1 in harzburgites are enriched in LREEs and LILEs relative to Cpx1 in lherzolites (Fig. 6). In addition, secondary vermicular or fine-grained clinopyroxenes and orthopyroxenes (Fig. 3a–c) were more often observed between porphyroclastic minerals in harzburgites than in lherzolites (Fig. 3e, f), suggesting that the harzburgites and lherzolites were affected by different degrees of melt-rock interaction.

Orthopyroxene incompatible element (e.g. non-fluid-mobile LREE) contents should gradually decrease as coexisting spinel Cr# increases (Bodinier and Godard, 2014; Warren, 2016). Here, orthopyroxenes in harzburgites exhibit pronounced LREE and LILE enrichments relative to those in lherzolites (Fig. 6). These affinities indicate that clinopyroxene LREE and LILE concentrations in harzburgites were substantially affected by melt-rock interaction. The whole-rock LREE contents of lherzolites show minor enrichments of La to Pr (Xiong et al., 2017), whereas no such enrichment is observed in clinopyroxenes (Fig. 6a). These inconsistent whole-rock and mineral-specific trace element features in lherzolites may contribute to post-melt flux being too low (Niu, 2004). Therefore, we conclude that the YZO harzburgites were subjected to a greater degree of melt-rock metasomatism than the lherzolites.

Journal Pre-proof

### 5.3 Thermal history of the YZO peridotites

Our calculated equilibration temperatures of the YZO lherzolites and harzburgites show notable differences (Fig. 9g, h). Combined, the group I lherzolites yielded $T_{BKN}$ = 884–977 °C (median 935 °C) and $T_{REE}$ = 994–1162 °C (median 1110 °C), whereas the group II lherzolite and harzburgites yielded $T_{BKN}$ = 836–977 °C (median 917 °C) and $T_{REE}$ = 991–1218 °C (median 1137 °C). The Ca-in-Opx geothermometer yielded equilibration temperatures ($T_{Ca\text{-}in\text{-}Opx}$) for harzburgites, group I lherzolites, and group II lherzolites of 918–997 °C, 901–958 °C, and 882–1154 °C, respectively. The $T_{Ca\text{-}in\text{-}Opx}$ values obtained from harzburgites span a broad range of temperatures, whereas the $T_{BKN}$ values calculated using Cpx-Opx mineral pairs are more uniform (though still spanning a range of more than 200 °C). Therefore, we will use $T_{BKN}$, the temperature obtained from the major element concentrations, for further discussion.

Previous studies have consistently shown that forearc peridotites exhibit notably lower equilibration temperatures than other oceanic mantle peridotites (Parkinson and Pearce, 1998; Zanetti et al., 2006). Dygert and Liang (2015) reported that SSZ ophiolites have lower closure temperatures than either abyssal peridotites or MOR-affinity ophiolites. They interpreted these low SSZ closure temperatures as reflecting long cooling histories, and higher closure temperatures as dominated by hydrothermal circulation and/or rapid cooling events (Dygert and Liang, 2015). However, more recent studies concluded that high closure temperatures also occur in forearc peridotites. For example, Secchiari et al. (2022) obtained higher temperatures ($T_{Ca\text{-}in\text{-}Opx}$ = 903–1185 °C) in New Caledonia forearc harzburgites than Pirard et al. (2013; $T_{Ca\text{-}in\text{-}Opx}$ = 953–970 °C), and Wu et al. (2022) found that both lherzolites ($T_{REE}$ = 1104–1429 °C) and harzburgites ($T_{REE}$ = 1019–1210 °C) derived from the Mirdita ophiolite also exhibit high closure temperatures. Here, the YZO lherzolites have slightly lower $T_{REE}$ values than the harzburgites (Fig. 9h), suggesting that the harzburgites record relatively higher cooling temperatures than the lherzolites. The large difference between $T_{REE}$ and $T_{BKN}$ suggests rapid cooling, because the closure to diffusion also relates to the cooling rate (Liang et al., 2013, 2021). We did not observe clear relationship between major element contents (e.g., $TiO_2$ and $Al_2O_3$) and $T_{REE}$ in clinopyroxenes (Fig. 10a, b), indicating that there is no discernible link between temperature and the degree of partial melting.

In a comparison of different tectonic environments around the world, mantle xenoliths and subcontinental peridotites exhibit nearly identical $T_{BKN}$ and $T_{REE}$ distributions (Fig. 9), indicating

that they underwent protracted slow cooling. The thermal features of (cold) subcontinental peridotites are distinct from other tectonic settings because they exhibit significantly lower $T_{REE}$ and $T_{BKN}$ values. The ophiolitic peridotites and abyssal peridotites exhibit low $T_{BKN}$ values but high $T_{REE}$ values, suggesting that they cooled faster than mantle xenoliths and subcontinental peridotites. The $T_{BKN}$ and $T_{REE}$ values estimated herein for the YZO peridotites overlap with the SSZ rather than MOR ophiolites (Fig. 9), indicating that the YZO peridotites record well-established SSZ thermal or cooling histories.

As an application of the $T_{BKN}$ and $T_{REE}$ estimates, Dygert and Liang (2015) used Dodson's (1973) thermodynamic equation to build closure temperature curves and calculate cooling rates for peridotites and mafic cumulates from different tectonic settings (including MOR, SSZ, and sub-continental) around the world. Here, we used the same method to calculate the cooling rate of lherzolites and harzburgites in the YZO. The cooling rates of group I lherzolites are similar to those of group II lherzolites at 0.05–0.5 °C/yr, similar to those of harzburgites extend to cooling rates of 0.01–0.5 °C/yr (Fig. 10d), indicating that the lherzolites and harzburgites did experience the exact same thermal processes. The YZO lherzolites and harzburgites plot within the area of overlap between the SSZ, MOR, and abyssal peridotite fields (Fig. 10), which is consistent with our statistical results (Fig. 9) and cooling rates of ophiolitic peridotites from the Samail and Yukon areas (Fig. 10d; Dygert et al., 2017; Canil et al., 2019). The absence of thick crust overlying abyssal peridotites, and thus a lack of thermal insulation, might be expected to result in differences compared to ophiolitic peridotites from SSZ environments. However, there are no significant differences between the $T_{REE}$ and $T_{BKN}$ distributions of abyssal peridotites and MOR or SSZ ophiolitic peridotites (Fig. 10d), indicating that the thickness of the overlying crust has no pronounced effect on the cooling rate of the oceanic mantle (Dygert et al., 2017). In addition, the cooling rates of peridotite samples from SSZ settings have been proposed to be similar to those of oceanic mantle peridotites (Dygert and Liang, 2015), further supporting our observation. Therefore, in general, the cooling rates of mantle peridotites exhibit no significant relationship with tectonic environment, whether SSZ, MOR, or abyssal. In contrast, the local geodynamic and thermal events may play a vital role. Importantly, our results indicate that the REE-in-pyroxene geospeedometry of Dygert et al. (2017) cannot completely distinguish cooling rates in these different tectonic settings.

Journal Pre-proof

### 5.4 The origin and evolution of the YZO

Recent studies have proposed that the YZO originated within a forearc environment (An et al., 2014; Huang et al., 2015; Maffione et al., 2015; Xiong, 2016; Xiong et al., 2017; Dai et al., 2021). For example, Xiong (2016) and Xiong et al. (2017) reported pyroxene compositions and Nd-Hf isotopic data for the Zedang harzburgites and lherzolites of the easternYZO and suggested that they formed in the forearc *via* multi-stage accretion. Based on a comprehensive field, petrological, geochronological, and geochemical investigation of mafic to felsic rocks in the Xigaze ophiolite (central YZO), Dai et al. (2021) concluded that the various rocks were generated in a single transient subduction initiation event in a forearc setting. In addition, the YZO samples record subsolidus temperatures, consistent with forearc thermal structure (van Keken et al., 2019). Peridotite melting in such conditions necessarily involves aqueous fluids to lower solidus temperatures. Therefore, the high degree of harzburgite partial melting compared to lherzolite could indicate that they were intensively metasomatized in a forearc environment. Furthermore, numerous models have been proposed to explain the origin of lherzolites and harzburgites, as outlined in the following paragraphs.

In subduction settings, lherzolites might form by: (1) the trapping and preservation of abyssal peridotites in the forearc region (Batanova and Sobolev, 2000; Choi et al., 2008; Arai et al., 2018); (2) the refertilization of mantle wedge peridotites by melt impregnation (Bryant et al., 2007; Scambelluri et al., 2006; Mitchell and Grove, 2016); (3) the rapid upwelling and cooling of the asthenospheric mantle (Xiong, 2016; Xiong et al., 2017); and/or (4) a low degree of partial melting of the depleted MORB mantle in the forearc area during subduction initiation (Ewart and Hawkesworth, 1987; Ulrich et al., 2010; Whattam and Stern, 2011; Stern et al., 2012; Marchesi et al., 2016). No distinct lithological demarcation between lherzolites and harzburgites in the YZO was discovered in the field, indicating that the YZO lherzolites were not trapped from old lithosphere, nor were they later accreted from the upwelling asthenospheric mantle. In addition, the petrological and geochemical features of the YZO lherzolites show a low degree of melt-rock interaction, suggesting that they were not formed by the percolation of fertile melt. We therefore conclude that the lherzolites observed herein were produced within a forearc spreading environment resulting from the initiation of subduction during the Early Cretaceous.

Turning to the YZO harzburgites, four models have been proposed for their formation. In the

first, the harzburgites formed at slow- or ultraslow-spreading MORs, as evidenced by their structural similarities to the ultraslow Southwest Indian Ridge, MORB-type crustal rocks, and the Ligurian ophiolite (Nicolas et al., 1981; Girardeau and Mercier, 1988; Pearce et al., 1988; Wu et al., 2014; C.Z. Liu et al., 2014; T. Liu et al., 2016; Zhang et al., 2016). In the second, the harzburgites formed in a forearc spreading setting through rapid accretion during subduction initiation from ~130 to 120 Ma (Malpas et al., 2003; Dai et al., 2013; An et al., 2014; Huang et al., 2015; Maffione et al., 2015). In the third, the harzburgites were initially generated in a MOR setting and subsequently modified in the SSZ (Zhou et al., 1996, 2005; Aitchison et al., 2000; Malpas et al., 2003; Dubois-Côté et al., 2005; Liu et al., 2010; Dai et al., 2011; Xu et al., 2011; Hébert et al., 2012; Su et al., 2015). The fourth model demonstrated that the harzburgites formed through asthenospheric upwelling during protracted accretion (Xiong, 2016; Xiong et al., 2017). As discussed above, the observed mineral major and trace element compositions in the YZO harzburgites might generated in a SSZ setting. Furthermore, our study highlights a gradual increase in the extent of depletion from lherzolites to harzburgites in the YZO peridotites.

Geodynamic models indicate that the YZO experienced a phase of forearc extension and margin-basin closure during Middle to Late Jurassic (~174–130 Ma), followed by intra-oceanic subduction initiation during the Early Cretaceous (~130 Ma; Dai et al., 2021). The same authors proposed that rollback of the sinking slab induced extension in the forearc of the overriding plate, leading to the Cretaceous subduction initiation; the rapidly retreating Neo-Tethyan oceanic slab was forced to subduct, leading to extension of the overriding plate and mantle upwelling (Dai et al., 2021). Continued subduction eventually led to the proto arc-continent (Zedang arc and Asian continent) collision, which finally resulted in the overthrusting of the ophiolitic units onto the Asian continental margin ~120 Ma, forming the YZO (Xiong, 2016; Dai et al., 2013, 2021).

In this framework, our geothermometry results may be explained as reflecting the short residence times (shorter than ~10 Ma) of the depleted mantle in the forearc region, followed by fast emplacement due to obduction (Fig. 11). Therefore, we speculate that the evolution of the YZO peridotites can be divided into two stages. During the early stage, a subduction initiation event in the front of the Gangdese arc was induced by the rollback of the Neo-Tethyan slab during the Early Cretaceous (Dai et al., 2021), and the associated upwelling of asthenospheric materials was responsible for emplacing the principal portion of the lherzolites at the forearc spreading center (Fig. 11a). The MORB-like basalts were formed at this time by decompression melting of

the fertile mantle. During the late stage, as subduction continued, the previously emplaced lherzolites were depleted by the large influx of slab fluids. As depletion intensified, most lherzolites were exhausted and developed into harzburgites that then experienced melt-rock interaction and were eventually obducted to the front of the Gangdese arc. Nonetheless, some of the previous lherzolites were necessarily preserved within the harzburgites (Fig. 11b).

## 6. Conclusions

We studied the melt extraction, closure temperatures, and cooling rates for mantle peridotites in the YZO. The YZO peridotites underwent varying degrees of partial melting, all of which display similar thermal or cooling histories. Based on our high quality major and trace element data in minerals from lherzolites and harzburgites in the YZO, as well as previous literature data and field observations, we drew the following main conclusions:

(1) Two groups of lherzolites are distinguished by their geochemical features. Group I lherzolites underwent 8–9% partial melting in the spinel field, whereas group II lherzolites and harzburgites experienced 5% dry melting in the garnet phase, followed by 6–9% dry and 9–16% partial melting in the spinel field, respectively. We speculate that such multi stage and larger degrees of partial melting might have occurred in a forearc environment.

(2) The lherzolites record a similar cooling temperature to the harzburgites, suggesting that the lherzolites and harzburgites have similar thermal or cooling histories. Generally, the equilibration temperatures of the YZO peridotites are similar to those of worldwide SSZ and lower than MOR ophiolites and abyssal peridotites. Therefore, we tentatively interpret that the YZO peridotites have thermal or cooling history pointing to SSZ affinity.

(3) We proposed a two-stage model for the formation of the YZO ophiolite. The lherzolites were formed in the forearc spreading center, induced by rollback of the subducting slab during the Early Cretaceous subduction initiation. As subduction continued, the majority of lherzolites were depleted by the influx of abundant slab fluids, eventually developing into the YZO harzburgites.

## Acknowledgements

We are grateful to Editor Sonja Aulbach and the anonymous reviewers for their helpful comments and suggestions. This study was supported by funding from National Natural Science Foundation of China (No. 42121002), 111 project (No. B18048) and the Agence Nationale de la Recherche (ANR) CARBioNic “ANR-22-CE49-0001-01”. This is CUGB petrogeochemical

contribution PGC201587.

## References

Aitchison, J.C., Badengzhu, Davis, A.M., Liu, J., Luo, H., Malpas, J.G., McDermid, I.R.C., Wu, H., Ziabrev, S.V., Zhou, M., 2000. Remnants of a Cretaceous intra-oceanic subduction system within the Yarlung–Zangbo suture (southern Tibet). Earth and Planetary Science Letters 183, 231–244. https://doi.org/10.1016/S0012-821X(00)00287-9

Aldanmaz, E., Schmidt, M.W., Gourgaud, A., Meisel, T., 2009. Mid-ocean ridge and supra-subduction geochemical signatures in spinel–peridotites from the Neotethyan ophiolites in SW Turkey: Implications for upper mantle melting processes. Lithos 113, 691–708. https://doi.org/10.1016/j.lithos.2009.03.010

Aldanmaz, E., van Hinsbergen, D.J.J., Yıldız-Yüksekol, Ö., Schmidt, M.W., McPhee, P.J., Meisel, T., Güçtekin, A., Mason, P.R.D., 2020. Effects of reactive dissolution of orthopyroxene in producing incompatible element depleted melts and refractory mantle residues during early fore-arc spreading: constraints from ophiolites in eastern Mediterranean. Lithos 360–361, 105438. https://doi.org/10.1016/j.lithos.2020.105438

Allégre, C.J., Courtillot, V., Tapponnier, P., Hirn, A., Mattauer, M., Coulon, C., Jaeger, J.J., Achache, J., Schärer, U., Marcoux, J., Burg, J.P., Girardeau, J., Armijo, R., Gariépy, C., Göpel, C., Tindong, L., Xuchang, X., Chenfa, C., Guangqin, L., Baoyu, L., Jiwen, T., Naiwen, W., Guoming, C., Tonglin, H., Xibin, W., Wanming, D., Huaibin, S., Yougong, C., Ji, Z., Hongrong, Q., Peisheng, P., Songchan, W., Bixiang, W., Yaoxiu, Z., Xu, R., 1984. Structure and evolution of the Himalaya–Tibet orogenic belt. Nature 307, 17–22. https://doi.org/10.1038/307017a0

An, W., Hu, X., Garzanti, E., BouDagher-Fadel, M.K., Wang, J., Sun, G., 2014. Xigaze forearc basin revisited (South Tibet): Provenance changes and origin of the Xigaze Ophiolite. GSA Bulletin 126, 1595–1613. https://doi.org/10.1130/B31020.1

Arai, S., 1994. Characterization of spinel peridotites by olivine-spinel compositional relationships: Review and interpretation. Chemical Geology 113, 191–204. https://doi.org/10.1016/0009-2541(94)90066-3

Arai, S., Abe, N., Ishimaru, S., 2007. Mantle peridotites from the Western Pacific. Gondwana Research, Island Arcs: Past and Present 11, 180–199. https://doi.org/10.1016/j.gr.2006.04.004

Arai, S., Tamura, A., Miura, M., Seike, K., 2018. Abyssal Peridotite as a Component of Forearc Mantle: Inference from a New Mantle Xenolith Suite of Bankawa in the Southwest Japan Arc. Minerals 8, 540. https://doi.org/10.3390/min8110540

Aulbach, S., Sun, J., Tappe, S., Höfer, H. E., Gerdes, A., 2017. Volatile-rich metasomatism in the cratonic mantle beneath SW Greenland: link to kimberlites and mid-lithospheric discontinuities. Journal of Petrology 58(12), 2311-2338. https://doi.org/10.1093/petrology/egy009

Batanova, V.G., Sobolev, A.V., 2000. Compositional heterogeneity in subduction-related mantle peridotites, Troodos massif, Cyprus. Geology 28, 55–58. https://doi.org/10.1130/0091-7613(2000)28<55:CHISMP>2.0.CO;2

Birner, S.K., Warren, J.M., Cottrell, E., Davis, F.A., Kelley, K.A., Falloon, T.J., 2017. Forearc

Peridotites from Tonga Record Heterogeneous Oxidation of the Mantle following Subduction Initiation. Journal of Petrology 58, 1755–1780. https://doi.org/10.1093/petrology/egx072

Bizimis, M., Salters, V.J.M., Bonatti, E., 2000. Trace and REE content of clinopyroxenes from supra-subduction zone peridotites. Implications for melting and enrichment processes in island arcs. Chemical Geology 165, 67–85. https://doi.org/10.1016/S0009-2541(99)00164-3

Bodinier, J.-L., Godard, M., 2014. 3.4 - Orogenic, Ophiolitic, and Abyssal Peridotites, in: Holland, H.D., Turekian, K.K. (Eds.), Treatise on Geochemistry (Second Edition). Elsevier, Oxford, pp. 103–167. https://doi.org/10.1016/B978-0-08-095975-7.00204-7

Brey, G.P., Köhler, T., 1990. Geothermobarometry in Four-phase Lherzolites II. New Thermobarometers, and Practical Assessment of Existing Thermobarometers. Journal of Petrology 31, 1353–1378. https://doi.org/10.1093/petrology/31.6.1353

Brunelli, D., Seyler, M., 2010. Asthenospheric percolation of alkaline melts beneath the St. Paul region (Central Atlantic Ocean). Earth and Planetary Science Letters 289, 393–405. https://doi.org/10.1016/j.epsl.2009.11.028

Bryant, J.A., Yogodzinski, G.M., Churikova, T.G., 2007. Melt-mantle interactions beneath the Kamchatka arc: Evidence from ultramafic xenoliths from Shiveluch volcano. Geochemistry, Geophysics, Geosystems 8. https://doi.org/10.1029/2006GC001443

Canil, D., Grundy, R., Johnston, S.T., 2019. Thermal history of the Donjek harzburgite massif in ophiolite from Yukon, Canada with implications for the cooling of oceanic mantle lithosphere. Lithos 328–329, 33–42. https://doi.org/10.1016/j.lithos.2019.01.001

Chen, J.-B., Zeng, Z.-M., 2007. Metasomatism of harzburgites in the southern of the Mariana Forearc: trace element characteristics of clinopyroxene and hornblende. Earth Science 37, 720-727 (in Chinese with English abstract).

Choi, S.H., Shervais, J.W., Mukasa, S.B., 2008. Supra-subduction and abyssal mantle peridotites of the Coast Range ophiolite, California. Contributions to Mineralogy and Petrology 156, 551. https://doi.org/10.1007/s00410-008-0300-6

Coleman, R.G., 1977. Ophiolites: New York. Springer Verlag 220.

Dai, J.G., Wang, C.S., Hébert, R., Santosh, M., Li, Y.L., Xu, J.Y., 2011. Petrology and geochemistry of peridotites in the Zhongba ophiolite, Yarlung Zangbo Suture Zone: Implications for the Early Cretaceous intra-oceanic subduction zone within the Neo-Tethys. Chemical Geology 288, 133–148. https://doi.org/10.1016/j.chemgeo.2011.07.011

Dai, J.G., Wang, C.S., Polat, A., Santosh, M., Li, Y.L., Ge, Y.K., 2013. Rapid forearc spreading between 130 and 120Ma: Evidence from geochronology and geochemistry of the Xigaze ophiolite, southern Tibet. Lithos 172–173, 1–16. https://doi.org/10.1016/j.lithos.2013.03.011

Dai, J.G., Wang, C.S., Zhu, D.C., Li, Y.L., Zhong, H.T., Ge, Y.K., 2015, Multi-stage volcanic activities and geodynamic evolution of the Lhasa terrane during the Cretaceous: Insights from the Xigaze forearc basin: Lithos, v. 218, p. 127–140, https://doi.org/10.1016/j.lithos.2015.01.019.

Dai, J.G., Wang, C.S., Stern, R.J., Yang, K., Shen, J., 2021. Forearc magmatic evolution during subduction initiation: Insights from an Early Cretaceous Tibetan ophiolite and comparison with the Izu-Bonin-Mariana forearc. GSA Bulletin 133, 753–776.

https://doi.org/10.1130/B35644.1

Dewey, J.F., Bird, J.M., 1971. The origin and emplacement of the ophiolite suite: Appalachian ophiolites in Newfoundland: Journal of Geophysical Research 76, 3179–3206. https://doi.org/10.1029/JB076i014p03179.

Dilek, Y., Furnes, H., 2011. Ophiolite genesis and global tectonics: Geochemical and tectonic fingerprinting of ancient oceanic lithosphere. GSA Bulletin 123, 387–411. https://doi.org/10.1130/B30446.1

Dilek, Y., & Furnes, H., 2019. Tethyan ophiolites and Tethyan seaways. Journal of the Geological Society 176(5), 899-912. https://doi.org/10.1144/jgs2019-129

Dilek, Y., Moores, E. M., 1990. Regional tectonics of the eastern Mediterranean ophiolites. In Troodos 1987. Symposium 295-309

Dilek, Y., Furnes, H., Shallo, M., 2007. Suprasubduction zone ophiolite formation along the periphery of Mesozoic Gondwana. Gondwana Research 11, 453–475. https://doi.org/10.1016/j.gr.2007.01.005

Dodson, M.H., 1973. Closure temperature in cooling geochronological and petrological systems. Contributions to Mineralogy and Petrology 40, 259–274. https://doi.org/10.1007/BF00373790

Dubois-Côté, V., Hébert, R., Dupuis, C., Wang, C.S., Li, Y.L., Dostal, J., 2005. Petrological and geochemical evidence for the origin of the Yarlung Zangbo ophiolites, southern Tibet. Chemical Geology 214, 265–286. https://doi.org/10.1016/j.chemgeo.2004.10.004

Dygert, N., Liang, Y., 2015. Temperatures and cooling rates recorded in REE in coexisting pyroxenes in ophiolitic and abyssal peridotites. Earth and Planetary Science Letters 420, 151–161. https://doi.org/10.1016/j.epsl.2015.02.042

Dygert, N., Kelemen, P.B., Liang, Y., 2017. Spatial variations in cooling rate in the mantle section of the Samail ophiolite in Oman: Implications for formation of lithosphere at mid-ocean ridges. Earth and Planetary Science Letters 465, 134–144. https://doi.org/10.1016/j.epsl.2017.02.038

Ewart, A., Hawkesworth, C.J., 1987. The Pleistocene-Recent Tonga-Kermadec Arc Lavas: Interpretation of New Isotopic and Rare Earth Data in Terms of a Depleted Mantle Source Model. Journal of Petrology 28, 495–530. https://doi.org/10.1093/petrology/28.3.495

Eyuboglu, Y., Dilek, Y., Bozkurt, E., Bektas, O., Rojay, B., Sen, C., 2010. Structure and geochemistry of an Alaskan-type ultramafic–mafic complex in the Eastern Pontides, NE Turkey. Gondwana Research, A Tribute to Miyashiro 18, 230–252. https://doi.org/10.1016/j.gr.2010.01.008

Fryer, P., Pearce, J.A., Stokking, L.B., et al. (Eds.), 1992. Proceedings of the Ocean Drilling Program, 125 Scientific Results, Proceedings of the Ocean Drilling Program. Ocean Drilling Program. https://doi.org/10.2973/odp.proc.sr.125.1992

Girardeau, J., Mercier, J.-C.C., 1988. Petrology and texture of the ultramafic rocks of the Xigaze ophiolite (Tibet): constraints for mantle structure beneath slow-spreading ridges. Tectonophysics 147, 33–58. https://doi.org/10.1016/0040-1951(88)90146-1

Girardeau, J., Mercier, J.C.C., Xibin, W., 1985. Petrology of the mafic rocks of the Xigaze ophiolite, Tibet: Implications for the genesis of the oceanic lithosphere. Contributions to Mineralogy and Petrology 90, 4, 309–321. https://doi.org/10.1007/BF00384710

Gong, X.-H., Shi, R.-D., Griffin, W.L., Huang, Q.-S., Xiong, Q., Chen, S.-S., Zhang, M., O'Reilly,

S.Y., 2016. Recycling of ancient subduction-modified mantle domains in the Purang ophiolite (southwestern Tibet). Lithos 262, 11–26. https://doi.org/10.1016/j.lithos.2016.06.025

Hanghøj, K., Kelemen, P.B., Hassler, D., Godard, M., 2010. Composition and Genesis of Depleted Mantle Peridotites from the Wadi Tayin Massif, Oman Ophiolite; Major and Trace Element Geochemistry, and Os Isotope and PGE Systematics. Journal of Petrology 51, 201–227. https://doi.org/10.1093/petrology/egp077

Hébert, R., Huot, F., Wang, C.S., Liu, Z.F., 2003. Yarlung Zangbo ophiolites (southern Tibet) revisited: Geodynamic implications from the mineral record, in Dilek, Y., and Robinson, P.T., eds., Ophiolites in Earth History. Geological Society [London] Special Publication 218, 165–190. https://doi.org/10.1144/GSL. SP.2003.218.01.10

Hébert, R., Bezard, R., Guilmette, C., Dostal, J., Wang, C.S., Liu, Z.F., 2012. The Indus–Yarlung Zangbo ophiolites from Nanga Parbat to Namche Barwa syntaxes, southern Tibet: First synthesis of petrology, geochemistry, and geochronology with incidences on geodynamic reconstructions of Neo-Tethys. Gondwana Research, Plate Tectonics of Asia: Geological and Geophysical Constraints 22, 377–397. https://doi.org/10.1016/j.gr.2011.10.013

Hellebrand, E., Snow, J.E., Dick, H.J.B., Hofmann, A.W., 2001. Coupled major and trace elements as indicators of the extent of melting in mid-ocean-ridge peridotites. Nature 410, 677–681. https://doi.org/10.1038/35070546

Hellebrand, E., Snow, J.E., Hoppe, P., Hofmann, A.W., 2002. Garnet-field melting and late-stage refertilization in 'residual'abyssal peridotites from the Central Indian Ridge. Journal of Petrology 43(12), 2305-2338. https://doi.org/10.1093/petrology/43.12.2305

Hellebrand, E., Snow, J.E., Mostefaoui, S., Hoppe, P., 2005. Trace element distribution between orthopyroxene and clinopyroxene in peridotites from the Gakkel Ridge: a SIMS and NanoSIMS study. Contributions to Mineralogy and Petrology 150, 486–504. https://doi.org/10.1007/s00410-005-0036-5

Huang, W., van Hinsbergen, D.J.J., Maffione, M., Orme, D.A., Dupont-Nivet, G., Guilmette, C., Ding, L., Guo, Z., Kapp, P., 2015. Lower Cretaceous Xigaze ophiolites formed in the Gangdese forearc: Evidence from paleomagnetism, sediment provenance, and stratigraphy. Earth and Planetary Science Letters 415, 142–153. https://doi.org/10.1016/j.epsl.2015.01.032

Ishikawa, A., Kaneko, Y., Kadarusman, A., Ota, T., 2007. Multiple generations of forearc mafic–ultramafic rocks in the Timor–Tanimbar ophiolite, eastern Indonesia. Gondwana Research, Island Arcs: Past and Present 11, 200–217. https://doi.org/10.1016/j.gr.2006.04.007

Ji, W.-Q., Wu, F.-Y., Chung, S.-L., Li, J.-X., Liu, C.-Z., 2009. Zircon U–Pb geochronology and Hf isotopic constraints on petrogenesis of the Gangdese batholith, southern Tibet. Chemical Geology 262, 229–245. https://doi.org/10.1016/j.chemgeo.2009.01.020

Jochum, K.P., Willbold, M., Raczek, I., Stoll, B., Herwig, K., 2005. Chemical Characterisation of the USGS Reference Glasses GSA-1G, GSC-1G, GSD-1G, GSE-1G, BCR-2G, BHVO-2G and BIR-1G Using EPMA, ID-TIMS, ID-ICP-MS and LA-ICP-MS. Geostandards and Geoanalytical Research 29, 285–302. https://doi.org/10.1111/j.1751-908X.2005.tb00901.x

Jochum, K.P., Weis, U., Stoll, B., Kuzmin, D., Yang, Q., Raczek, I., Jacob, D.E., Stracke, A.,

Birbaum, K., Frick, D.A., Günther, D., Enzweiler, J., 2011. Determination of Reference Values for NIST SRM 610–617 Glasses Following ISO Guidelines. Geostandards and Geoanalytical Research 35, 397–429. https://doi.org/10.1111/j.1751-908X.2011.00120.x

Johnson, K. T., 1998. Experimental determination of partition coefficients for rare earth and high-field-strength elements between clinopyroxene, garnet, and basaltic melt at high pressures. Contributions to Mineralogy and Petrology 133(1-2), 60-68. https://doi.org/10.1007/s004100050437

Johnson, K.T.M., Dick, H.J.B., Shimizu, N., 1990. Melting in the oceanic upper mantle: An ion microprobe study of diopsides in abyssal peridotites. J. Geophys. Res. 95, 2661. https://doi.org/10.1029/JB095iB03p02661

Kaczmarek, M.A., Müntener, O., 2008. Juxtaposition of melt impregnation and high-temperature shear zones in the upper mantle; field and petrological constraints from the Lanzo Peridotite (Northern Italy). Journal of petrology 49(12), 2187-2220. https://doi.org/10.1093/petrology/egn065

Kelemen, P.B., Dick, H.J.B., Quick, J.E., 1992. Formation of harzburgite by pervasive melt/rock reaction in the upper mantle. Nature 358, 635–641. http://doi.org/10.1038/358635a0

Kimura, J.-I., Kawabata, H., 2014. Trace element mass balance in hydrous adiabatic mantle melting: The Hydrous Adiabatic Mantle Melting Simulator version 1 (HAMMS1). Geochemistry, Geophysics, Geosystems 15, 2467–2493. https://doi.org/10.1002/2014GC005333

Lagabrielle, Y., and Cannat, M., 1990. Alpine Jurassic ophiolites resemble the modern central Atlantic basement. Geology 18, 319–322. https://doi.org/10.1130/0091-7613(1990)018<0319:AJORTM>2.3.CO;2

Le Roux, V., Bodinier, J.-L., Tommasi, A., Alard, O., Dautria, J.-M., Vauchez, A., Riches, A.J.V., 2007. The Lherz spinel lherzolite: Refertilized rather than pristine mantle. Earth and Planetary Science Letters 259, 599–612. https://doi.org/10.1016/j.epsl.2007.05.026

Liang, Y., Sun, C., Yao, L., 2013. A REE-in-two-pyroxene thermometer for mafic and ultramafic rocks. Geochimica et Cosmochimica Acta 102, 246–260. https://doi.org/10.1016/j.gca.2012.10.035

Liang, Y., Ji, Z., Liu, I., 2021. What can we learn from REE abundancesin clinopyroxene and orthopyroxene in residual mantle peridotites? Contributions to Mineralogy and Petrology 176, 24. https://doi.org/10.1007/s00410-021-01780-x

Lindsley, D.H., Andersen, D.J., 1983. A two-pyroxene thermometer. Journal of Geophysical Research: Solid Earth 88(S02), A887-A906. https://doi.org/10.1029/JB088iS02p0A887

Liu, C.-Z., Wu, F.-Y., Wilde, S.A., Yu, L.-J., Li, J.-L., 2010. Anorthitic plagioclase and pargasitic amphibole in mantle peridotites from the Yungbwa ophiolite (southwestern Tibetan Plateau) formed by hydrous melt metasomatism. Lithos 114, 413–422. https://doi.org/10.1016/j.lithos.2009.10.008

Liu, C.-Z., Zhang, C., Yang, L.-Y., Zhang, L.-L., Ji, W.-Q., Wu, F.-Y., 2014. Formation of gabbronorites in the Purang ophiolite (SW Tibet) through melting of hydrothermally altered mantle along a detachment fault. Lithos 205, 127–141. https://doi.org/10.1016/j.lithos.2014.06.019

Liu, T., Wu, F.-Y., Zhang, L.-L., Zhai, Q.-G., Liu, C.-Z., Ji, W.-B., Zhang, C., Xu, Y., 2016. Zircon U-Pb geochronological constraints on rapid exhumation of the mantle peridotite of the

Xigaze ophiolite, southern Tibet. Chemical Geology 443, 67–86. https://doi.org/10.1016/j.chemgeo.2016.09.015

Liu, T., Wu, F. Y., Liu, C. Z., Zhang, C., Ji, W. B., Xu, Y., 2019. Reconsideration of Neo-Tethys evolution constrained from the nature of the Dazhuqu ophiolitic mantle, southern Tibet. Contributions to Mineralogy and Petrology 174, 1-23. https://doi.org/10.1007/s00410-019-1557-7

Liu, T., Liu, C.-Z., Wu, F.-Y., Dick, H.J.B., Ji, W.-B., Zhang, C., Zhang, W.-Q., Zhang, Z.-Y., Xu, Y., 2021. The Xigaze ophiolite: fossil ultraslow-spreading ocean lithosphere in the Tibetan Plateau. Journal of the Geological Society 178, jgs2020-208. https://doi.org/10.1144/jgs2020-208

Liu, Y., Hu, Z., Gao, S., Günther, D., Xu, J., Gao, C., Chen, H., 2008. In situ analysis of major and trace elements of anhydrous minerals by LA-ICP-MS without applying an internal standard. Chemical Geology 257, 34–43. https://doi.org/10.1016/j.chemgeo.2008.08.004

MacGregor, I.D., 2015. Empirical geothermometers and geothermobarometers for spinel peridotite phase assemblages. International Geology Review 57, 1940–1974. https://doi.org/10.1080/00206814.2015.1045307

Maffione, M., van Hinsbergen, D.J.J., Koornneef, L.M.T., Guilmette, C., Hodges, K., Borneman, N., Huang, W., Ding, L., Kapp, P., 2015. Forearc hyperextension dismembered the south Tibetan ophiolites. Geology 43, 475–478. https://doi.org/10.1130/G36472.1

Malpas, J., Zhou, M.-F., Robinson, P.T., Reynolds, P.H., 2003. Geochemical and geochronological constraints on the origin and emplacement of the Yarlung Zangbo ophiolites, Southern Tibet. Geological Society, London, Special Publications 218, 191–206. https://doi.org/10.1144/GSL.SP.2003.218.01.11

Marchesi, C., Garrido, C.J., Proenza, J.A., Hidas, K., Varas-Reus, M.I., Butjosa, L., Lewis, J.F., 2016. Geochemical record of subduction initiation in the sub-arc mantle: Insights from the Loma Caribe peridotite (Dominican Republic). Lithos 252–253, 1–15. https://doi.org/10.1016/j.lithos.2016.02.009

Martin, B., Fyfe, W. S., 1970. Some experimental and theoretical observations on the kinetics of hydration reactions with particular reference to serpentinization. Chemical Geology 6, 185-202. https://doi.org/10.1016/0009-2541(70)90018-5

McKenzie, D., O'Nions, R.K., 1991. Partial Melt Distributions from Inversion of Rare Earth Element Concentrations. Journal of Petrology 32, 1021–1091. https://doi.org/10.1093/petrology/32.5.1021

Metcalf, R. V., Shervais, J. W., Wright, J. E., 2008. Suprasubduction-zone ophiolites: Is there really an ophiolite conundrum? Special Papers-Geological Society of America 438, 191. https://doi.org/10.1130/2008.2438(07)

Mitchell, A.L., Grove, T.L., 2016. Experiments on melt–rock reaction in the shallow mantle wedge. Contributions to Mineralogy and Petrology 171, 107. https://doi.org/10.1007/s00410-016-1312-2

Moores, E.M., Kellogg, L.H., Dilek, Y., 2000. Tethyan ophiolites, mantle convection, and tectonic "historical contingency": A resolution of the "ophiolite conundrum." Special Paper of the Geological Society of America 349, 3–12. https://doi.org/10.1130/0-8137-2349-3.3

Müntener, O., Pettke, T., Desmurs, L., Meier, M., Schaltegger, U., 2004. Refertilization of mantle peridotite in embryonic ocean basins: trace element and Nd isotopic evidence and

implications for crust–mantle relationships. Earth and Planetary Science Letters 221, 293–308. https://doi.org/10.1016/S0012-821X(04)00073-1

Nicolas, A., 1989, Structure of Ophiolites and Dynamics of Oceanic Lithosphere: Dordrecht, the Netherlands. Kluwer Academic Publishers 367.

Nicolas, A., Girardeau, J., Marcoux, J., Dupre, B., Xibin, W., Yougong, C., Haixiang, Z., Xuchang, X., 1981. The Xigaze ophiolite (Tibet): a peculiar oceanic lithosphere. Nature 294, 414–417. https://doi.org/10.1038/294414a0

Niu, Y., 2004. Bulk-rock Major and Trace Element Compositions of Abyssal Peridotites: Implications for Mantle Melting, Melt Extraction and Post-melting Processes Beneath Mid-Ocean Ridges. Journal of Petrology 45, 2423–2458. https://doi.org/10.1093/petrology/egh068

Parkinson, I.J., Pearce, J.A., 1998. Peridotites from the Izu–Bonin–Mariana Forearc (ODP Leg 125): Evidence for Mantle Melting and Melt–Mantle Interaction in a Supra-Subduction Zone Setting 39, 42.

Paton, C., Hellstrom, J., Paul, B., Woodhead, J., Hergt, J., 2011. Iolite: Freeware for the visualisation and processing of mass spectrometric data. J. Anal. At. Spectrom. 26, 2508–2518. https://doi.org/10.1039/C1JA10172B

Pearce, J.A., Wanming, D., Chengfa, C., Shackleton, R.M., Dewey, J.F., Jixiang, Y., 1988. The ophiolites of the Tibetan Geotraverses, Lhasa to Golmud (1985) and Lhasa to Kathmandu (1986). Philosophical Transactions of the Royal Society of London. Series A, Mathematical and Physical Sciences 327, 215–238. https://doi.org/10.1098/rsta.1988.0127

Piccardo, G.B., Zanetti, A., Müntener, O., 2007. Melt/peridotite interaction in the Southern Lanzo peridotite: Field, textural and geochemical evidence. Lithos, Melting, Metasomatism and Metamorphic Evolution in the Lithospheric Mantle 94, 181–209. https://doi.org/10.1016/j.lithos.2006.07.002

Pirard, C., Hermann, J., O'Neill, H.ST.C., 2013. Petrology and Geochemistry of the Crust–Mantle Boundary in a Nascent Arc, Massif du Sud Ophiolite, New Caledonia, SW Pacific. Journal of Petrology 54, 1759–1792. https://doi.org/10.1093/petrology/egt030

Prinzhofer, A., Allègre, C.J., 1985. Residual peridotites and the mechanisms of partial melting. Earth and Planetary Science Letters 74, 251–265. https://doi.org/10.1016/0012-821X(85)90025-1

Putirka, K.D., 2008. Thermometers and barometers for volcanic systems. Reviews in mineralogy and geochemistry 69(1), 61-120. https://doi.org/10.2138/rmg.2008.69.3

Robinson, P. T., Bai, W.J., Malpas, J., Yang, J.S., Zhou, M.F., Fang, Q.S., Hu, X.F., Cameron, S., and Staudigel. H., 2004. Ultra-high pressure minerals in the Luobusa Ophiolite, Tibet, and their tectonic implications, in Aspects of the tectonic evolution of China, Geological Society, London, Special Publications 226, 247–271. https://doi.org/10.1144/GSL.SP.2004.226.01.14

Ruskov, T., Spirov, I., Georgieva, M., Yamamoto, S., Green, H.W., McCammon, C.A., Dobrzhinetskaya, L.F., 2010. Mössbauer spectroscopy studies of the valence state of iron in chromite from the Luobusa massif of Tibet: implications for a highly reduced deep mantle. Journal of Metamorphic Geology 28(5), 551-560. https://doi.org/10.1111/j.1525-1314.2010.00878.x

Salters, V.J.M., Stracke, A., 2004. Composition of the depleted mantle. Geochemistry, Geophysics, Geosystems 5. https://doi.org/10.1029/2003GC000597

Sano S, Kimura J. I., 2007. Clinopyroxene REE geochemistry of the Red Hills peridotite, New Zealand: interpretation of magmatic processes in the upper mantle and in the Moho transition zone. Journal of Petrology 48(1): 113-139. https://doi.org/10.1093/petrology/egl056

Scambelluri, M., Hermann, J., Morten, L., Rampone, E., 2006. Melt- versus fluid-induced metasomatism in spinel to garnet wedge peridotites (Ulten Zone, Eastern Italian Alps): clues from trace element and Li abundances. Contributions to Mineralogy and Petrology 151, 372–394. https://doi.org/10.1007/s00410-006-0064-9

Secchiari, A., Montanini, A., Bosch, D., Macera, P., Cluzel, D., 2016. Melt extraction and enrichment processes in the New Caledonia lherzolites: evidence from geochemical and Sr–Nd isotope data. Lithos 260, 28-43. https://doi.org/10.1016/j.lithos.2016.04.030

Secchiari, A., Montanini, A., Bosch, D., Macera, P., Cluzel, D., 2020. Sr, Nd, Pb and trace element systematics of the New Caledonia harzburgites: Tracking source depletion and contamination processes in a SSZ setting. Geoscience Frontiers 11, 37–55. https://doi.org/10.1016/j.gsf.2019.04.004

Secchiari, A., Montanini, A., Cluzel, D., 2022. Temperatures and cooling rates recorded by the New Caledonia ophiolite: Implications for cooling mechanisms in young forearc sequences. Geochemistry, Geophysics, Geosystems 23, e2021GC009859. https://doi.org/10.1029/2021GC009859

Seyler, M., Brunelli, D., Toplis, M.J., Mével, C., 2011. Multiscale chemical heterogeneities beneath the eastern Southwest Indian Ridge (52°E-68°E): Trace element compositions of along-axis dredged peridotites: CHEMICAL HETEROGENEITIES IN PERIDOTITES. Geochem. Geophys. Geosyst. 12, n/a-n/a. https://doi.org/10.1029/2011GC003585

Shervais, J.W., Jean, M.M., 2012. Inside the subduction factory: Modeling fluid mobile element enrichment in the mantle wedge above a subduction zone. Geochimica et Cosmochimica Acta 95, 270–285. https://doi.org/10.1016/j.gca.2012.07.006

Shi, R., Alard, O., Zhi, X., O'Reilly, S.Y., Pearson, N.J., Griffin, W.L., Zhang, M., Chen, X., 2007. Multiple events in the Neo-Tethyan oceanic upper mantle: Evidence from Ru–Os–Ir alloys in the Luobusa and Dongqiao ophiolitic podiform chromitites, Tibet. Earth and Planetary Science Letters 261, 33–48. https://doi.org/10.1016/j.epsl.2007.05.044

Shi, R.D., Huang, Q.S., Liu, D.L., Fan, S.Q., Zhang, X.R., Ding, L., Griffin, W.L., O'Reilly, S.Y., 2012. Recycling of ancient sub-continental lithospheric mantle constraints on the genesis of the ophiolitic podiform chromitites. Geological Review 58, 643–652.

Smith, A.G., 1993. Tectonic significance of the Hellenic–Dinaric ophiolites: Geological Society of London Special Publication 76, 213–245. https://doi.org/10.1144/GSL.SP.1993.076.01.10

Stern, R.J., Reagan, M., Ishizuka, O., Ohara, Y., Whattam, S., 2012. To understand subduction initiation, study forearc crust: To understand forearc crust, study ophiolites. Lithosphere 4, 469–483. https://doi.org/10.1130/L183.1

Su, B.X., Teng, F.Z., Hu, Y., Shi, R.D., Zhou, M.F., Zhu, B., Liu, F., Gong, X.H., Huang, Q.S., Xiao, Y., Chen, C., He, Y.S., 2015. Iron and magnesium isotope fractionation in oceanic lithosphere and sub-arc mantle: Perspectives from ophiolites. Earth and Planetary Science Letters 430, 523–532. https://doi.org/10.1016/j.epsl.2015.08.020

Sun, S.-s., McDonough, W.F., 1989. Chemical and isotopic systematics of oceanic basalts: implications for mantle composition and processes. Geological Society, London, Special Publications 42, 313–345. https://doi.org/10.1144/GSL.SP.1989.042.01.19

Taylor, W.R., 1998. An experimental test of some geothermometer and geobaro-meter formulations for upper mantle peridotites with application to the ther-mobarometry of fertile lherzolite and garnet websterite. Neues Jahrbuch für Mineralogie - Abhandlungen 381–408. https://doi.org/10.1127/njma/172/1998/381

Ulrich, M., Picard, C., Guillot, S., Chauvel, C., Cluzel, D., Meffre, S., 2010. Multiple melting stages and refertilization as indicators for ridge to subduction formation: The New Caledonia ophiolite. Lithos 115, 223–236. https://doi.org/10.1016/j.lithos.2009.12.011

Urann, B.M., Dick, H.J.B., Parnell-Turner, R., Casey, J.F., 2020. Recycled arc mantle recovered from the Mid-Atlantic Ridge. Nature communications 11(1), 3887. https://doi.org/10.1038/s41467-020-17604-8

van Keken, P., Wada, I., Sime, N., Abers, G., 2019. Thermal structure of the forearc in subduction zones: A comparison of methodologies. Geochemistry Geophysics Geosystems 20, 3268–3288. https://doi. org/10.1029/2019GC008334

Vernières, J., Godard, M., Bodinier, J.-L., 1997. A plate model for the simulation of trace element fractionation during partial melting and magma transport in the Earth's upper mantle. Journal of Geophysical Research: Solid Earth 102, 24771–24784. https://doi.org/10.1029/97JB01946

Walter, M.J., 1998. Melting of Garnet Peridotite and the Origin of Komatiite and Depleted Lithosphere. Journal of Petrology 39, 29–60. https://doi.org/10.1093/petroj/39.1.29

Wang, C., Li, X., Liu, Z., Li, Y., Jansa, L., Dai, J., Wei, Y., 2012. Revision of the Cretaceous–Paleogene stratigraphic framework, facies architecture and provenance of the Xigaze forearc basin along the Yarlung Zangbo suture zone. Gondwana Research, Plate Tectonics of Asia: Geological and Geophysical Constraints 22, 415–433. https://doi.org/10.1016/j.gr.2011.09.014

Wang, Y., Zeng, L., Asimow, P.D., Gao, L.E., Ma, C., Antoshechkina, P.M., Guo, C., Hou, K., Tang, S., 2018. Early Cretaceous high-Ti and low-Ti mafic magmatism in Southeastern Tibet: Insights into magmatic evolution of the Comei Large Igneous Province. Lithos 296–299, 396–411. https://doi.org/10.1016/j.lithos.2017.11.014

Warren, J.M., 2016. Global variations in abyssal peridotite compositions. Lithos 248–251, 193–219. https://doi.org/10.1016/j.lithos.2015.12.023

Warren, J.M., Shimizu, N., Sakaguchi, C., Dick, H.J.B., Nakamura, E., 2009. An assessment of upper mantle heterogeneity based on abyssal peridotite isotopic compositions. J. Geophys. Res. 114, B12203. https://doi.org/10.1029/2008JB006186

Wells, P.R.A., 1977. Pyroxene thermometry in simple and complex systems. Contr. Mineral. and Petrol. 62, 129–139. https://doi.org/10.1007/BF00372872

Whattam, S.A., Stern, R.J., 2011. The 'subduction initiation rule': a key for linking ophiolites, intra-oceanic forearcs, and subduction initiation. Contributions to Mineralogy and Petrology 162, 1031–1045. https://doi.org/10.1007/s00410-011-0638-z

Witt-Eickschen, G., Seck, H.A., 1991. Solubility of Ca and Al in orthopyroxene from spinel peridotite: an improved version of an empirical geothermometer. Contr. Mineral. and Petrol. 106, 431–439. https://doi.org/10.1007/BF00321986

Journal Pre-proof

Wu, F.Y., Liu, C.Z., Zhang, L.L., Zhang, C., Wang, J.G., Ji, W.Q., Liu, X.C., 2014. Yarlung Zangbo ophiolite: a critical updated view. Acta Petrol. Sin. 30, 293–325 (in Chinese with English abstract).

Wu, W., Yang, J., Zheng, J., Lian, D., Milushi, I., Yang, Y., Qiu, T., Rui, H., Guo, G., Dai, Z., Masoud, A. E. I., 2022. The earliest stage of mantle-melt evolution during subduction initiation: Evidence from the Neo-Tethyan Mirdita Ophiolite, Albania. Lithos 434, 106937. https://doi.org/10.1016/j.lithos.2022.106937

Xiong, Q., Griffin, W. L., Zheng, J. P., O'Reilly, S. Y., Pearson, N. J., Xu, B., Belousova, E. A., 2016. Southward trench migration at∼ 130–120 Ma caused accretion of the Neo-Tethyan forearc lithosphere in Tibetan ophiolites. Earth and Planetary Science Letters 438, 57-65. https://doi.org/10.1016/j.epsl.2016.01.014

Xiong, Q., Griffin, W.L., Zheng, J.-P., Pearson, N.J., O'Reilly, S.Y., 2017. Two-layered oceanic lithospheric mantle in a Tibetan ophiolite produced by episodic subduction of Tethyan slabs: TWO-LAYERED TETHYAN MANTLE IN TIBET. Geochemistry, Geophysics, Geosystems 18, 1189–1213. https://doi.org/10.1002/2016GC006681

Xu, X., Yang, J., Ba, D., Guo, G., Robinson, P.T., Li, J., 2011. Petrogenesis of the Kangjinla peridotite in the Luobusa ophiolite, Southern Tibet. Journal of Asian Earth Sciences, Subduction and exhumation history recorded in HP-UHP metamorphic rocks 42, 553–568. https://doi.org/10.1016/j.jseaes.2011.05.007

Yang, J. S., Dobrzhinetskaya, L., Bai, W. J., Fang, Q. S., Robinson, P.T., Zhang, J., Green, H.W., II, 2007. Diamond- and coesite-bearing chromitites from the Luobusa ophiolite, Tibet. Geology 35, 875–878. https://doi.org/10.1130/G23766A.1

Yang, J.S., Robinson, P.T., Dilek, Y., 2014. Diamonds in Ophiolites. Elements 10, 127–130. https://doi.org/10.2113/gselements.10.2.127

Yang, K., Dai, J.G, Shen, J., Jia, X.L., 2022. Episodic continental extension in eastern Gondwana during the mid-late mesozoic: insights from geochronology and geochemistry of mafic rocks in the Tethyan Himalaya. International Geology Review 1-18. https://doi.org/10.1080/00206814.2022.2045637

Yin, A., Harrison, T.M., 2000. Geologic Evolution of the Himalayan-Tibetan Orogen. Annual Review of Earth and Planetary Sciences 28, 211–280. https://doi.org/10.1146/annurev.earth.28.1.211

Zanetti, A., D'Antonio, M., Spadea, P., Raffone, N., Vannucci, R., Brugier, O., 2006. Petrogenesis of mantle peridotites from the Izu-Bonin-Mariana (IBM) forearc. Ofioliti 31(2), 189–206.

Zhao, M.S., Chen, Y.X., & Zheng, Y.F., 2021. Geochemical evidence for forearc metasomatism of peridotite in the Xigaze ophiolite during subduction initiation in Neo-Tethyan Ocean, south to Tibet. Lithos 380, 105896. https://doi.org/10.1016/j.lithos.2020.105896

Zhang, C., Liu, C.Z., Wu, F.Y., Zhang, L.L., Ji, W.Q., 2016. Geochemistry and geochronology of mafic rocks from the Luobusa ophiolite, South Tibet. Lithos, Recent advances on the tectonic and magmatic evolution of the Greater Tibetan Plateau: A Special Issue in Honor of Prof. Guitang Pan 245, 93–108. https://doi.org/10.1016/j.lithos.2015.06.031

Zhang, C., Liu, C.Z., Wu, F.Y., Ji, W.B., Liu, T., Xu, Y., 2017. Ultra-refractory mantle domains in the Luqu ophiolite (Tibet): petrology and tectonic setting. Lithos 286, 252-263. https://doi.org/10.1016/j.lithos.2017.05.021

Zhang, C., Liu, C.Z., Liu, T., Wu, F.Y., 2020. Evolution of mantle peridotites from the Luobusa

ophiolite in the Tibetan Plateau: Sr-Nd-Hf-Os isotope constraints. Lithos 362, 105477. https://doi.org/10.1016/j.lithos.2020.105477

Zhang, L.L., Zhu, D.C., Wang, Q., Zhao, Z.D., Liu, D., Xie, J.C., 2019. Late Cretaceous volcanic rocks in the Sangri area, southern Lhasa Terrane, Tibet: Evidence for oceanic ridge subduction. Lithos 326–327, 144–157. https://doi.org/10.1016/j.lithos.2018.12.023

Zhou, M.F., Robinson, P.T., Malpas, J., Li, Z., 1996. Podiform Chromitites in the Luobusa Ophiolite (Southern Tibet): Implications for Melt-Rock Interaction and Chromite Segregation in the Upper Mantle. Journal of Petrology 37, 3–21. https://doi.org/10.1093/petrology/37.1.3

Zhou, M.F., Robinson, P.T., Malpas, J., Edwards, S.J., Qi, L., 2005. REE and PGE Geochemical Constraints on the Formation of Dunites in the Luobusa Ophiolite, Southern Tibet. Journal of Petrology 46, 615–639. https://doi.org/10.1093/petrology/egh091

Zhu, D.C., Chung, S.L., Mo, X.X., Zhao, Z.D., Niu, Y., Song, B., Yang, Y.H., 2009. The 132 Ma Comei-Bunbury large igneous province: Remnants identified in present-day southeastern Tibet and southwestern Australia. Geology 37, 583–586. https://doi.org/10.1130/G30001A.1

Zhu, D.C., Zhao, Z.D., Niu, Y., Mo, X.X., Chung, S.L., Hou, Z.Q., Wang, L.Q., Wu, F.Y., 2011. The Lhasa Terrane: Record of a microcontinent and its histories of drift and growth. Earth and Planetary Science Letters 301, 241–255. https://doi.org/10.1016/j.epsl.2010.11.005

Zhu, D.C., Zhao, Z.D., Niu, Y., Dilek, Y., Hou, Z.Q., Mo, X.X., 2013. The origin and pre-Cenozoic evolution of the Tibetan Plateau. Gondwana Research 23, 1429–1454. https://doi.org/10.1016/j.gr.2012.02.002

## Figure Captions:

Figure 1. Geological sketch map of the Yarlung Zangbo ophiolite and adjacent tectonic units (south Tibet; modified after Dai et al., 2011). Major faults: GCT, Great Counter thrust; ZGT, Zhongba–Gyangze thrust; GT, Gangdese thrust.

Figure 2. Field photos of the Yarlung Zangbo ophiolitic peridotite. (a) Pyroxenite dike cutting harzburgite; (b) lherzolite outcrop; (c) harzburgite encrusted by weathered shells; (d) superficially exposed orthopyroxenes on harzburgite.

Figure 3. (a–f) Cross-polarized photomicrographs and (g–l) backscatter electron micrographs of the YZO peridotite. Red squares and arrows in (e) and (f) indicate the fields of view in (h) and (i), respectively. (a–c) Harzburgites contain porphyroclasts (e.g., Ol1, Opx1, Cpx1), and matrix assemblages (e.g., Ol2, Opx2, Cpx2, Serp); the harzburgite in (c) displays porphyroclastic and protogranular textures. (d–f) Cpx-Opx mineral pairs with clear boundaries; distinct Opx lamellae are present in the Cpx1 minerals. (g–l) Cpx-Opx mineral pairs shown as backscatter electron images. Abbreviations: Cpx, clinopyroxene; Opx, orthopyroxene; Ol, olivine; Spl, spinel; Serp, serpentine.

Figure 4. Variations of (a) Mg# *vs*. Cr# in spinel, (b) olivine Mg# *vs*. spinel Cr#, and (c) chondrite-

normalized Sm/Yb *vs*. Yb contents for clinopyroxene in the YZO peridotites. The olivine-spinel mantle array in (b) is after Arai (1994). The normalized values for chondrite and primitive mantle are from Sun and McDonough (1989). DMM represents spinel in the depleted MORB mantle (Salters and Stracke, 2004); FMM represents the fertile MORB mantle. The dunite and peridotite data in YZO are from Zhang et al. (2017), Liu et al. (2019).

Figure 5. Variations of (a) $Al_2O_3$ *vs*. $Cr_2O_3$ contents, (b) Mg# *vs*. $Al_2O_3$ content, (c) Mg# *vs*. $TiO_2$ content, (d) Mg# *vs*. $Na_2O$ content, (e) Mg# *vs*. $Cr_2O_3$ content, and (f) Mg# *vs*. Ca/Al for clinopyroxenes in the YZO peridotites. Blue, purple, and green symbols indicate harzburgites, group I lherzolites, and group II lherzolites, respectively. DMM represents clinopyroxene from the depleted MORB mantle (Salters and Stracke, 2004).

Figure 6. (a, c) Chondrite-normalized REE patterns and (b, d) primitive-mantle-normalized trace element patterns for the clinopyroxenes and orthopyroxenes in YZO (a, b) lherzolites (c, d) harzburgites. The normalization values for chondrites and the primitive mantle are from Sun and McDonough (1989). The field of abyssal peridotites is after Johnson et al. (1990), Brunelli and Seyler (2010), Hellebrand et al. (2005), Seyler et al. (2011), and Warren et al. (2009); that of SSZ peridotites is after Aldanmaz et al. (2020), Batanova and Sobolev (2000), Bizimis et al. (2000), Birner et al. (2017), and Dygert and Liang (2015); and that of Mariana forearc peridotites is after Fryer et al. (1992), Parkinson and Pearce (1998), and Chen and Zeng (2007).

Figure 7. Chondrite-normalized REE patterns for clinopyroxenes in the YZO (a, c) lherzolites and (b, d) harzburgites compared to those modeled after single-stage partial melting. The normalization values for chondrites are from Sun and McDonough (1989). DMM represents clinopyroxene from the depleted MORB mantle (Salters and Stracke, 2004). (a, b) Purple and (c, d) pink dashed curves represent the modeled REE compositions of residual clinopyroxenes after 1–25% of perfect non-modal fractional melting within spinel- and garnet-facies mantle, respectively, calculated using the modeling equations and starting mineral modes of Johnson et al. (1990), melt modes from Walter (1998), olivine-, orthopyroxene-, spinel-, and garnet-melt partition coefficients from McKenzie and O'Nions (1991), and clinopyroxene-melt partition coefficients from Vernières et al. (1997). The literature data of the clinopyroxene from the YZO are from Liu et al. (2012), Xiong et al. (2017), Zhang et al. (2017), Liu et al. (2019), Zhao et al. (2021).

Figure 8. Chondrite-normalized REE patterns for clinopyroxenes in the YZO (a) lherzolites and (b) harzburgites compared to those calculated after two-stage partial melting. The normalization values for chondrites are from Sun and McDonough (1989). DMM represents clinopyroxene from the depleted MORB mantle (Salters and Stracke, 2004). The purple dashed curves represent the modeled REE compositions of residual clinopyroxenes after an initial 5% partial melting in garnet-facies mantle and subsequent 1–18% perfect non-modal fractional melting in spinel-facies mantle, calculated using the modeling equations and starting mineral modes of Johnson et al. (1990), melt modes from Walter (1998), olivine-, orthopyroxene-, spinel-, and garnet-melt partition coefficients from McKenzie and O'Nions (1991), and clinopyroxene-melt partition coefficients from Vernières et al. (1997). Data sources for the literature are as in Figure 7.

Figure 9. Histograms for samples (a, b) of different lithologies from this study and (c–h) from different tectonic affinities, showing ranges of temperatures calculated using the REE-in-two-pyroxene thermometer (green) and the two-pyroxene major element thermometer of Brey and Köhler (1990) (black diagonal lines). Data in (c–g) are from Dygert and Liang (2015) and references therein.

Figure 10. Variations of (a) $Al_2O_3$ in clinopyroxenes, (b) $TiO_2$ in clinopyroxenes, (c) CaO in orthopyroxene, and (d) $T_{BKN}$ *vs.* $T_{REE}$ for the peridotites from the Yarlung Zangbo ophiolitic massif. The $T_{REE}$ error bars are 1σ standard deviations. We apply an uniform error of 30 °C to $T_{BKN}$. In (d), cooling curves (orange lines) are calculated for initial peak temperatures on the solidus ($T_0$) followed by cooling at various rates (in °C/yr, vertical black lines) to the final closure temperatures of $T_{REE}$ and $T_{BKN}$ for an orthopyroxene grain of radius 0.5 mm. These calculations follow the method and diffusion parameters for REE and Fe-Mg diffusion in pyroxenes outlined in Dygert et al. (2017). Also shown are values of $T_{REE}$ and $T_{BKN}$ calculated for the Yarlung Zangbo ophiolitic massif (symbols), and other SSZ and MOR ophiolites, and abyssal peridotites (pink, green, and orange fields, respectively) (after Dygert and Liang, 2015).

Figure 11. Tectonic model for the origin and tectonic evolution of the Yarlung Zangbo ophiolitic peridotites.

## Tables Caption:

Table S1. Major and trace element compositions of clinopyroxene, orthopyroxene, olivine, and spinel.

Table S2. Major and trace element compositions of the equilibrium pyroxene pairs used for geothermometer.

Journal Pre-proof

**Declaration of interests**

☒The authors declare that they have no known competing financial interests or personal relationships that could have appeared to influence the work reported in this paper.

☐The authors declare the following financial interests/personal relationships which may be considered as potential competing interests:

Journal Pre-proof

## Highlights

- The YZO lherzolite displays two different geochemical features and melting types.
- Two different partial melting processes between lherzolite and harzburgite.
- The ophiolitic peridotites display similar thermal features across different settings.
- The YZO lherzolite and harzburgite were formed in a forearc setting.

Journal Pre-proof

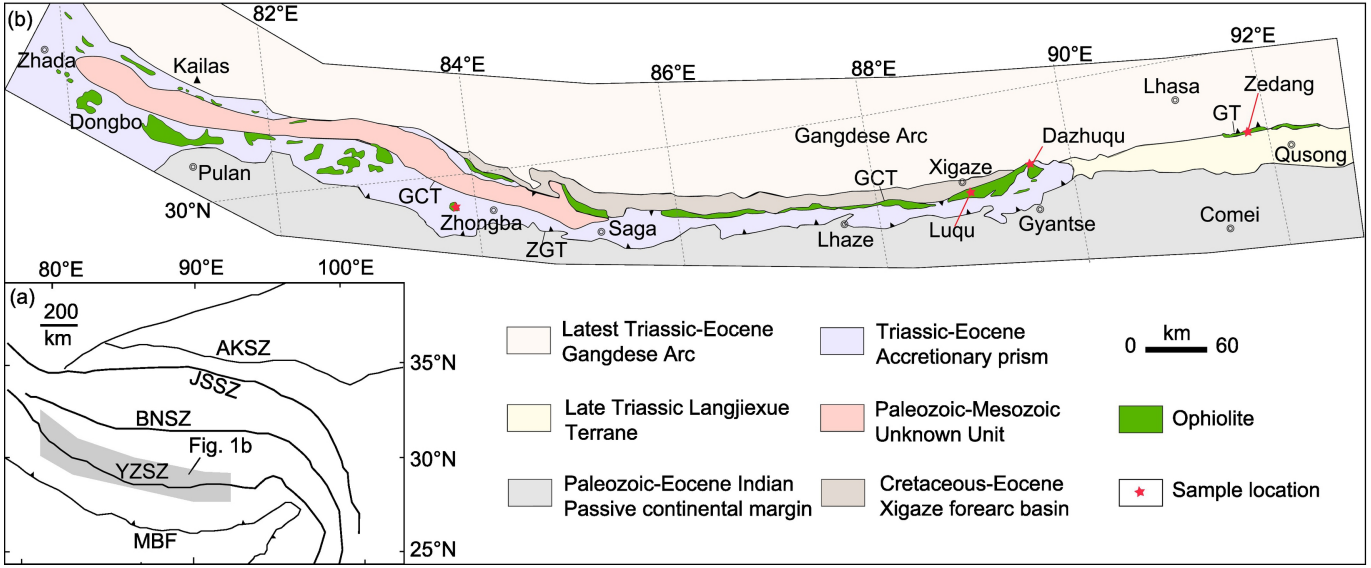
(b)
82°E
84°E
86°E
88°E
90°E
92°E
Zhada
Kailas
Dongbo
Pulan
30°N
GCT
Zhongba
ZGT
Saga
Gangdese Arc
GCT
Xigaze
Dazhuqu
Lhaze
Luqu
Gyantse
Lhasa
Zedang
GT
Qusong
Comei
80°E
90°E
100°E
(a)
200
km
AKSZ
JSSZ
BNSZ
Fig. 1b
YZSZ
MBF
35°N
30°N
25°N
Latest Triassic-Eocene
Gangdese Arc
Triassic-Eocene
Accretionary prism
0
km
60
Late Triassic Langjiexue
Terrane
Paleozoic-Mesozoic
Unknown Unit
Ophiolite
Paleozoic-Eocene Indian
Passive continental margin
Cretaceous-Eocene
Xigaze forearc basin
Sample location

Figure 1


Figure 2

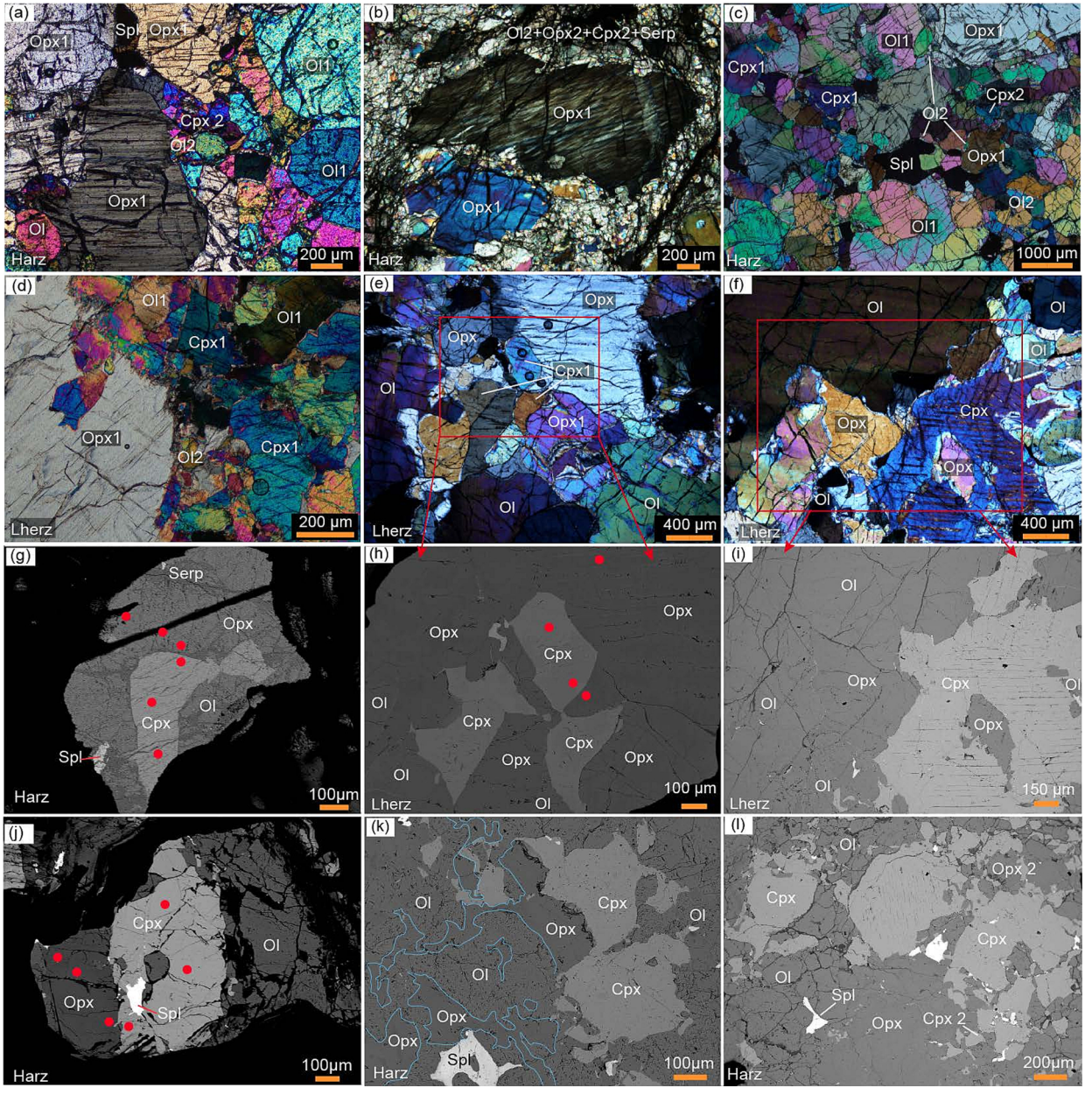
(a)
Opx1
Spl
Opx1
Ol1
Cpx 2
Ol2
Ol1
Opx1
Ol
Harz
200 μm
(b)
Ol2+Opx2+Cpx2+Serp
Opx1
Opx1
Harz
200 μm
(c)
Ol1
Opx1
Cpx1
Cpx1
Cpx2
Ol2
Spl
Opx1
Ol2
Ol1
Harz
1000 μm
(d)
Ol1
Ol1
Cpx1
Opx1
Ol2
Cpx1
Lherz
200 μm
(e)
Opx
Opx
Cpx1
Ol
Opx1
Ol
Ol
Lherz
400 μm
(f)
Ol
Ol
Ol
Cpx
Opx
Opx
Ol
Lherz
400 μm
(g)
Serp
Opx
Ol
Cpx
Spl
Harz
100μm
(h)
Opx
Opx
Cpx
Ol
Cpx
Cpx
Opx
Opx
Ol
Lherz
Ol
100 μm
(i)
Ol
Opx
Cpx
Ol
Ol
Opx
Ol
Lherz
150 μm
(j)
Cpx
Ol
Opx
Spl
Harz
100μm
(k)
Ol
Cpx
Opx
Ol
Ol
Cpx
Opx
Opx
Spl
Harz
100μm
(l)
Ol
Opx 2
Cpx
Cpx
Ol
Spl
Opx
Cpx 2
Harz
200μm

Figure 3

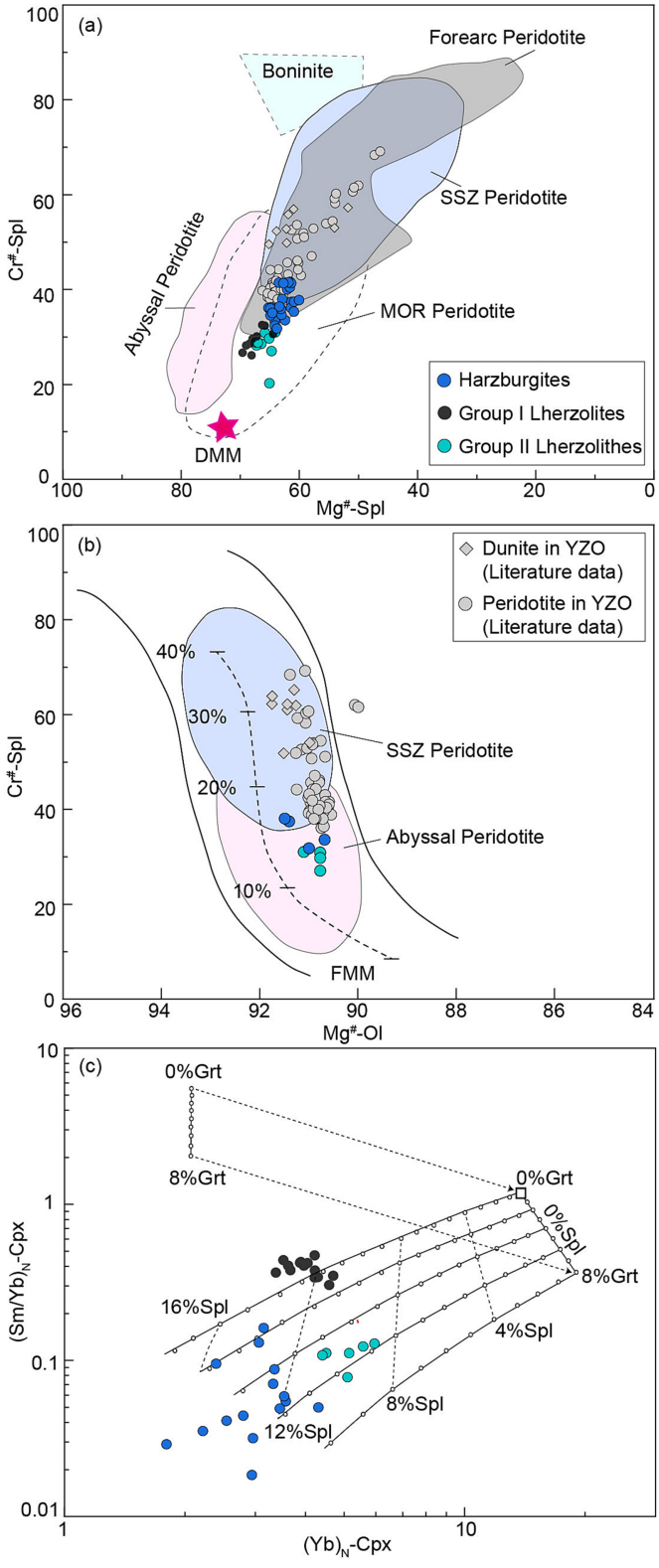
(a)
Forearc Peridotite
Boninite
SSZ Peridotite
Abyssal Peridotite
MOR Peridotite
Harzburgites
Group I Lherzolites
Group II Lherzolithes
DMM
Cr#-Spl
Mg#-Spl
(b)
Dunite in YZO (Literature data)
Peridotite in YZO (Literature data)
40%
30%
20%
10%
SSZ Peridotite
Abyssal Peridotite
FMM
Cr#-Spl
Mg#-Ol
(c)
0%Grt
8%Grt
0%Grt
0%Spl
8%Grt
16%Spl
4%Spl
8%Spl
12%Spl
(Sm/Yb)N-Cpx
(Yb)N-Cpx

Figure 4

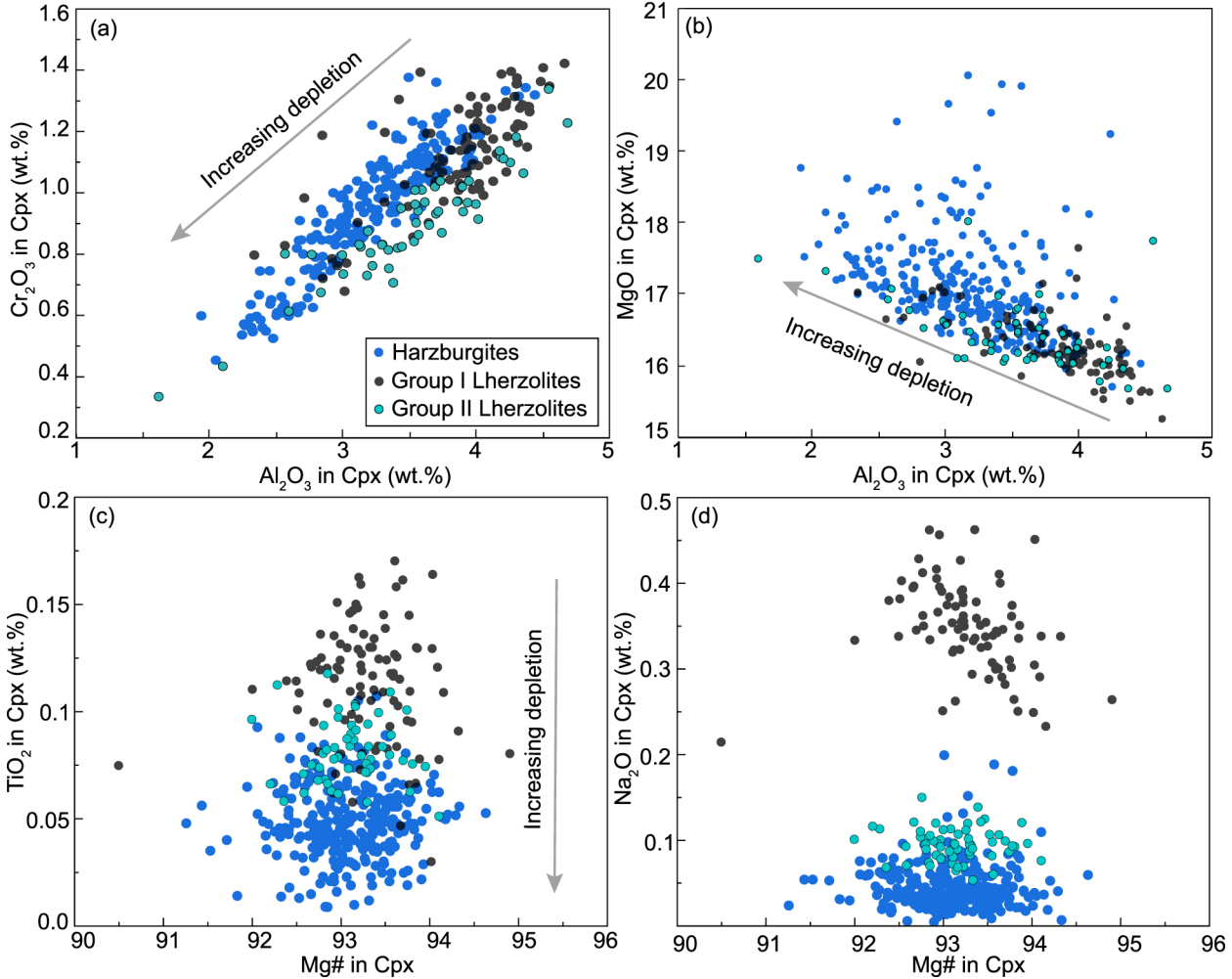
(a)
Increasing depletion
Cr2O3 in Cpx (wt.%)
Al2O3 in Cpx (wt.%)
Harzburgites
Group I Lherzolites
Group II Lherzolites
(b)
Increasing depletion
MgO in Cpx (wt.%)
Al2O3 in Cpx (wt.%)
(c)
Increasing depletion
TiO2 in Cpx (wt.%)
Mg# in Cpx
(d)
Na2O in Cpx (wt.%)
Mg# in Cpx

Figure 5

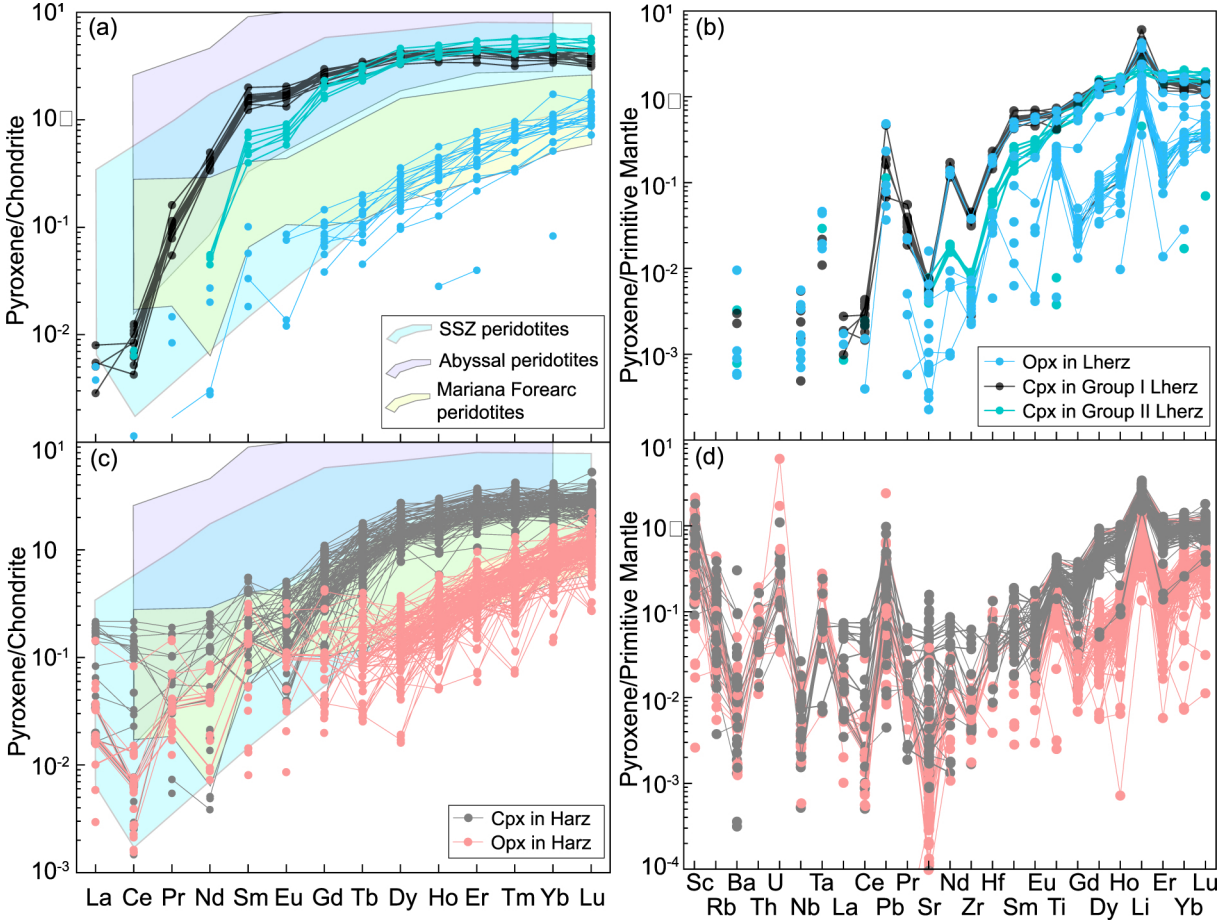
(a)
Pyroxene/Chondrite
SSZ peridotites
Abyssal peridotites
Mariana Forearc peridotites
(b)
Pyroxene/Primitive Mantle
Opx in Lherz
Cpx in Group I Lherz
Cpx in Group II Lherz
(c)
Pyroxene/Chondrite
Cpx in Harz
Opx in Harz
La Ce Pr Nd Sm Eu Gd Tb Dy Ho Er Tm Yb Lu
(d)
Pyroxene/Primitive Mantle
Sc Rb Ba Th U Nb Ta La Ce Pb Pr Sr Nd Zr Hf Sm Eu Ti Gd Dy Ho Li Er Yb Lu

Figure 6

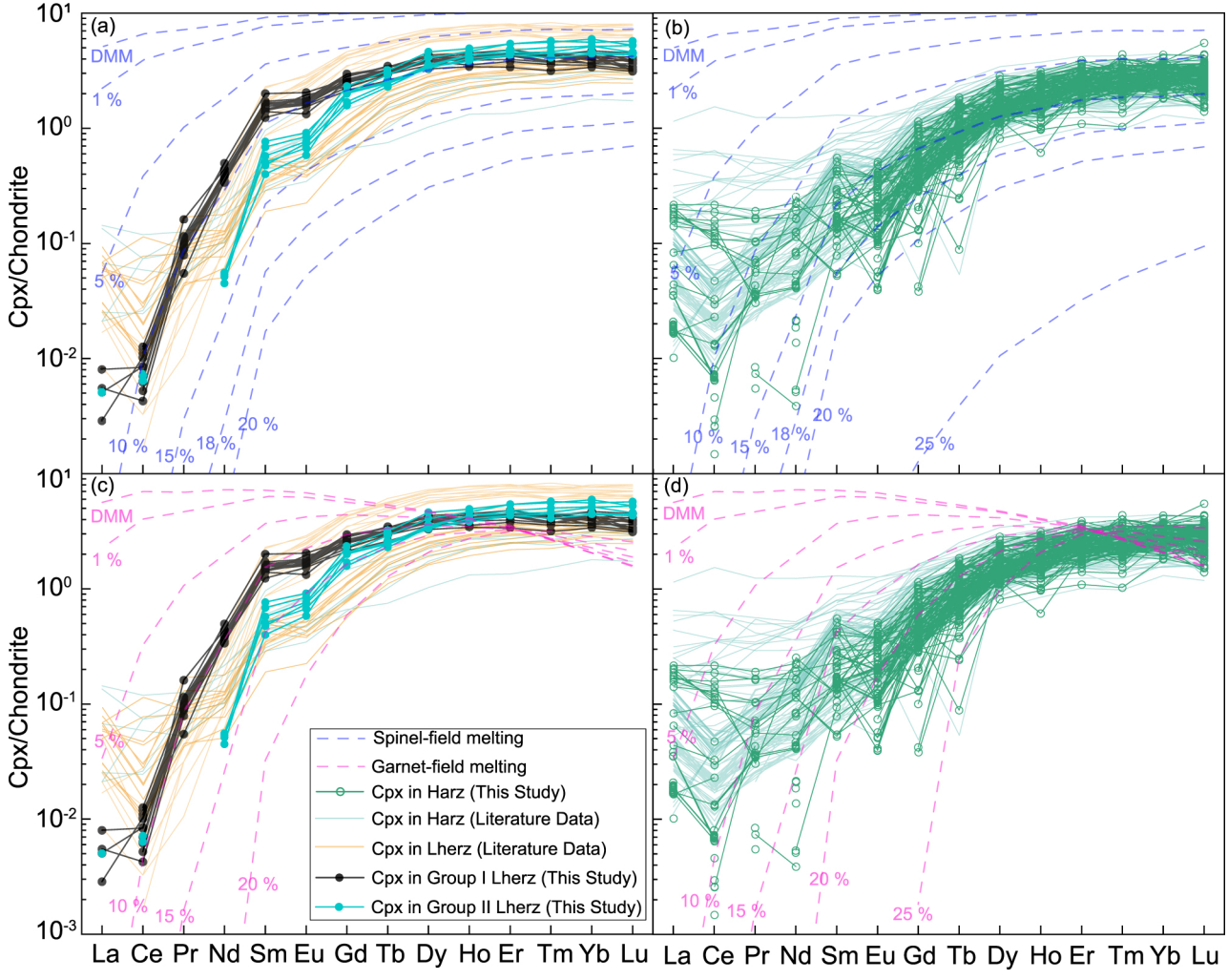
(a)
(b)
(c)
(d)
DMM
1 %
5 %
10 %
15 %
18 %
20 %
25 %
Cpx/Chondrite
La Ce Pr Nd Sm Eu Gd Tb Dy Ho Er Tm Yb Lu
Spinel-field melting
Garnet-field melting
Cpx in Harz (This Study)
Cpx in Harz (Literature Data)
Cpx in Lherz (Literature Data)
Cpx in Group I Lherz (This Study)
Cpx in Group II Lherz (This Study)

Figure 7

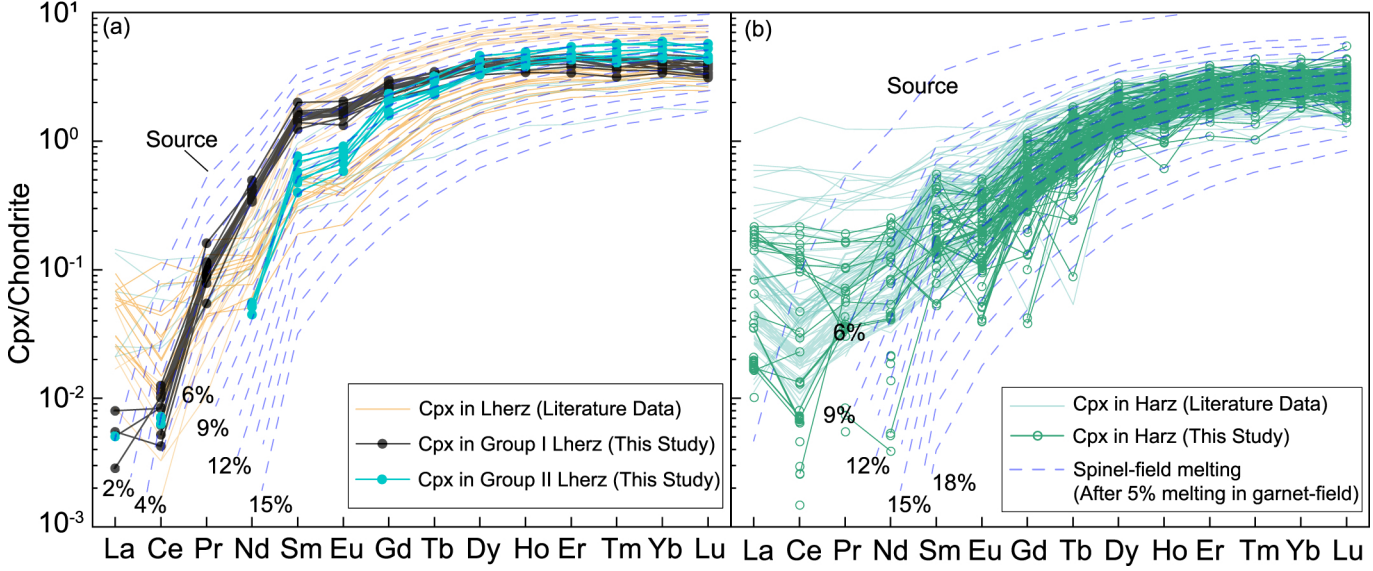
(a)
(b)
Source
Source
Cpx/Chondrite
$10^{1}$
$10^{0}$
$10^{-1}$
$10^{-2}$
$10^{-3}$
2%
4%
6%
9%
12%
15%
18%
Cpx in Lherz (Literature Data)
Cpx in Group I Lherz (This Study)
Cpx in Group II Lherz (This Study)
Cpx in Harz (Literature Data)
Cpx in Harz (This Study)
Spinel-field melting
(After 5% melting in garnet-field)
La Ce Pr Nd Sm Eu Gd Tb Dy Ho Er Tm Yb Lu
La Ce Pr Nd Sm Eu Gd Tb Dy Ho Er Tm Yb Lu

Figure 8

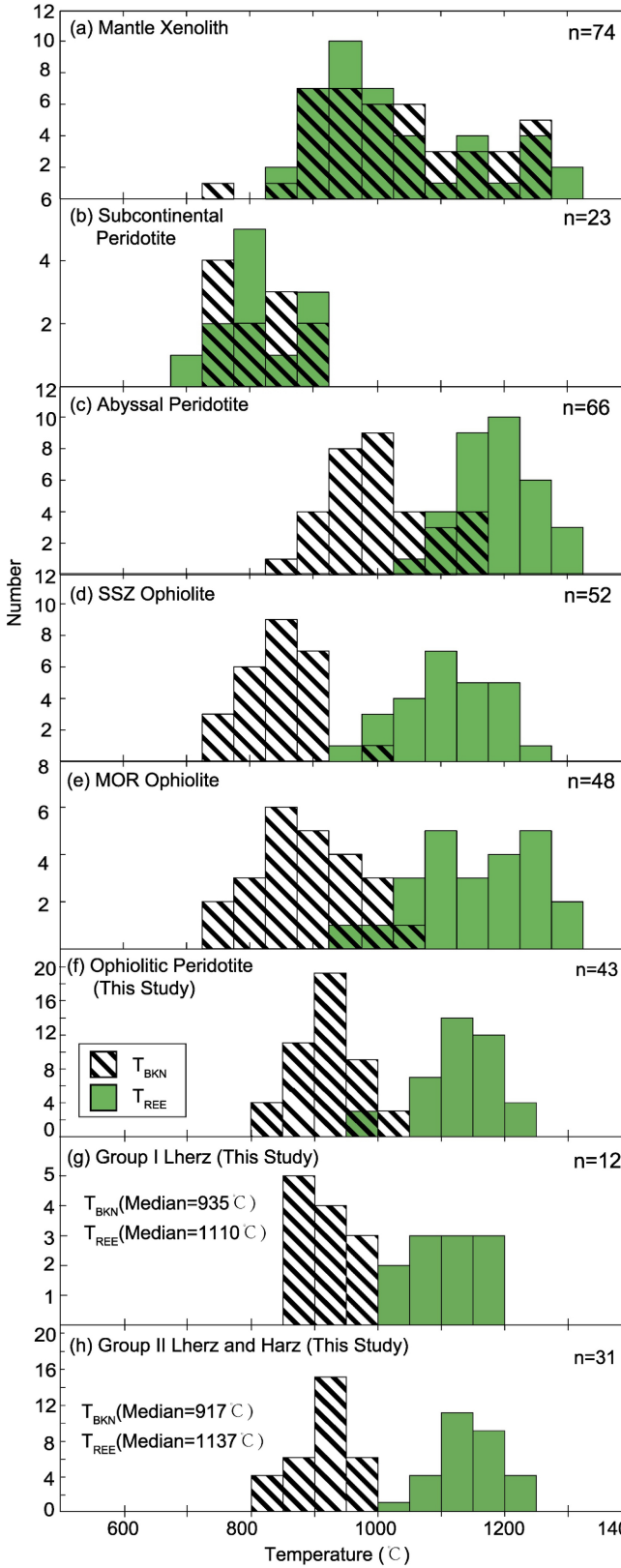
(a) Mantle Xenolith
n=74
(b) Subcontinental Peridotite
n=23
(c) Abyssal Peridotite
n=66
(d) SSZ Ophiolite
n=52
(e) MOR Ophiolite
n=48
(f) Ophiolitic Peridotite (This Study)
n=43
T_BKN
T_REE
(g) Group I Lherz (This Study)
n=12
T_BKN(Median=935℃)
T_REE(Median=1110℃)
(h) Group II Lherz and Harz (This Study)
n=31
T_BKN(Median=917℃)
T_REE(Median=1137℃)
Number
Temperature (℃)
600
800
1000
1200
1400

Figure 9

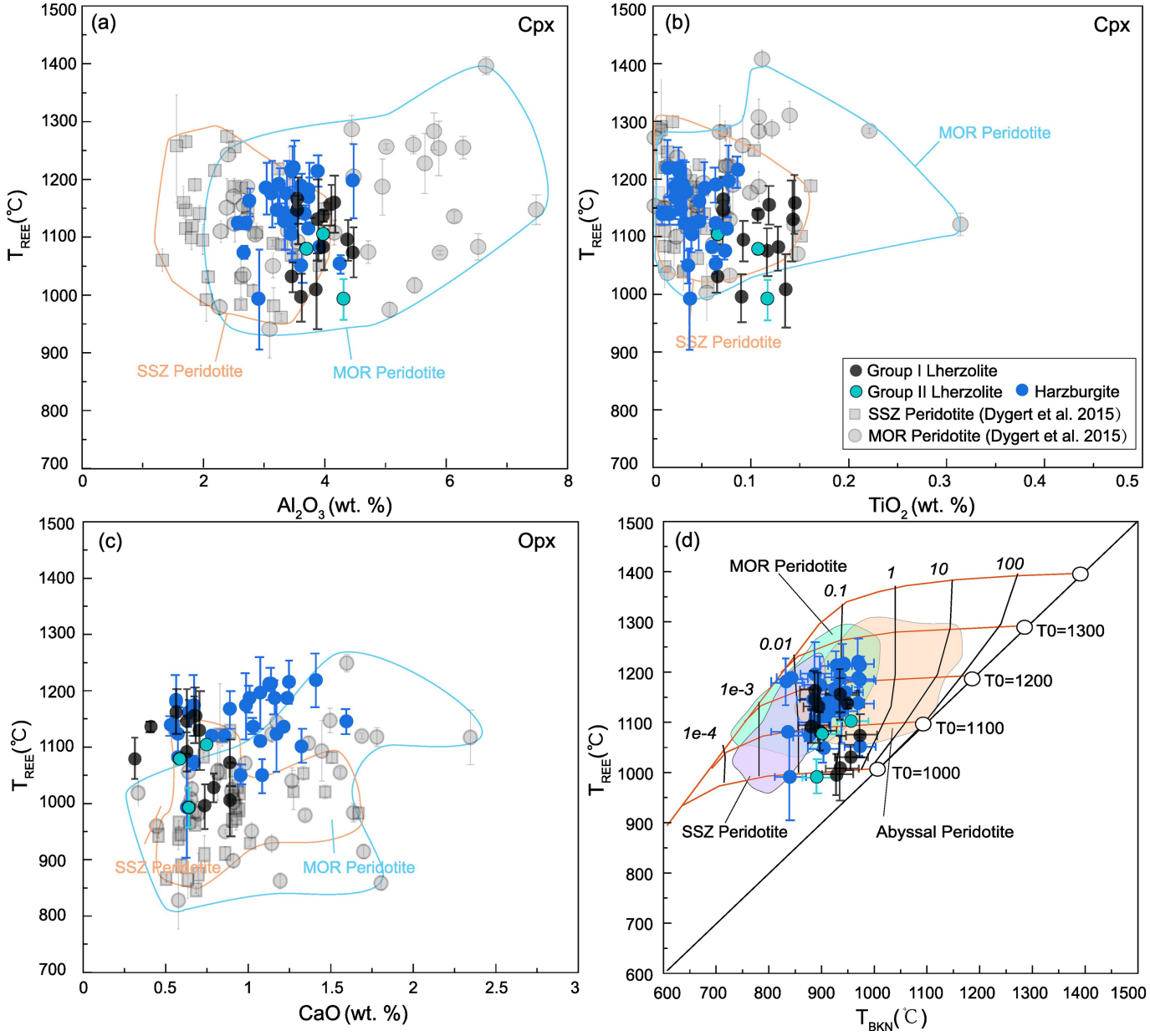
(a)
Cpx
SSZ Peridotite
MOR Peridotite
$T_{REE}$(℃)
$Al_2O_3$ (wt. %)
(b)
Cpx
MOR Peridotite
SSZ Peridotite
Group I Lherzolite
Group II Lherzolite
Harzburgite
SSZ Peridotite (Dygert et al. 2015)
MOR Peridotite (Dygert et al. 2015)
$TiO_2$ (wt. %)
(c)
Opx
SSZ Peridotite
MOR Peridotite
CaO (wt. %)
(d)
MOR Peridotite
0.1
1
10
100
0.01
1e-3
1e-4
T0=1300
T0=1200
T0=1100
T0=1000
SSZ Peridotite
Abyssal Peridotite
$T_{BKN}$(℃)

Figure 10

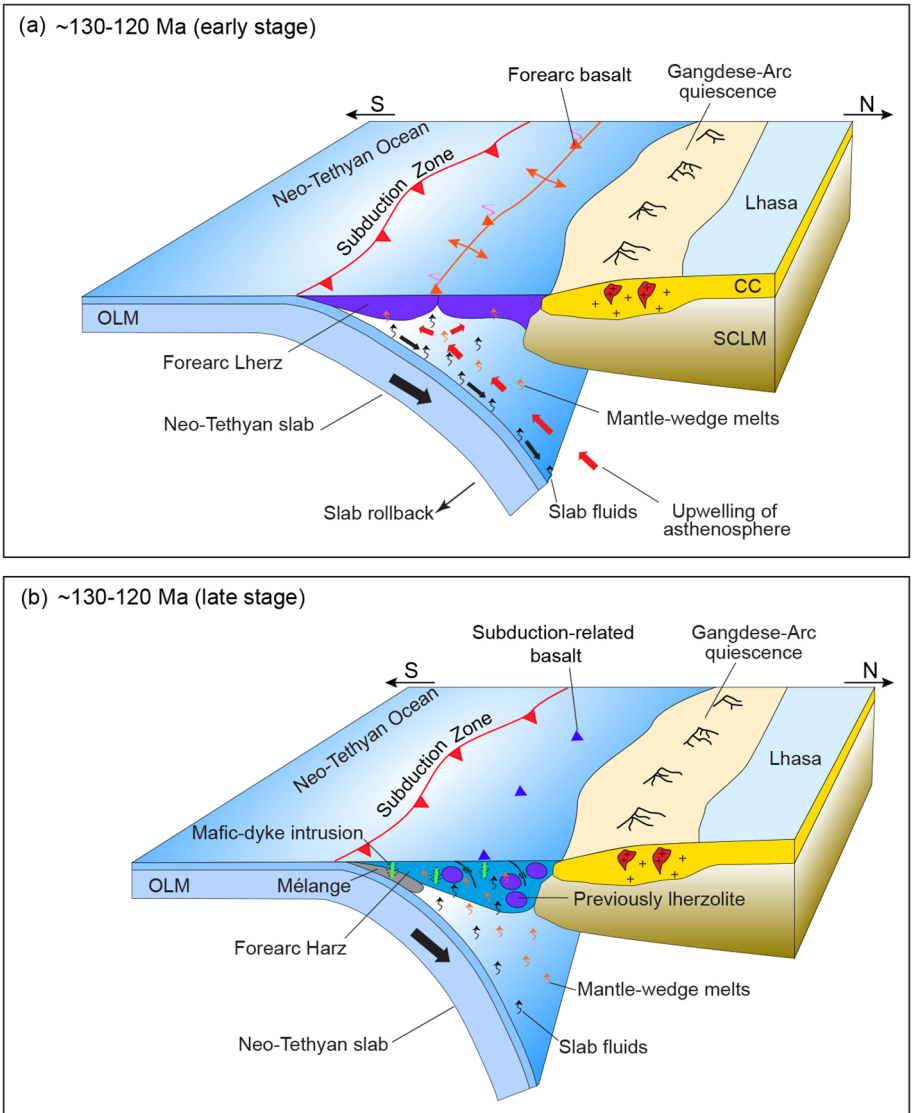
(a) ~130-120 Ma (early stage)
S
N
Forearc basalt
Gangdese-Arc quiescence
Neo-Tethyan Ocean
Subduction Zone
Lhasa
CC
SCLM
OLM
Forearc Lherz
Neo-Tethyan slab
Mantle-wedge melts
Slab rollback
Slab fluids
Upwelling of asthenosphere
(b) ~130-120 Ma (late stage)
Subduction-related basalt
Gangdese-Arc quiescence
S
N
Neo-Tethyan Ocean
Subduction Zone
Lhasa
Mafic-dyke intrusion
OLM
Mélange
Previously lherzolite
Forearc Harz
Mantle-wedge melts
Neo-Tethyan slab
Slab fluids

Figure 11